Ann. N.Y. Acad. Sci. ISSN 0077-8923

ANNALS OF THE NEW YORK ACADEMY OF SCIENCES
Special Issue: *Advancing Tools and Methods for Flexible Adaptation Pathways and Science Policy Integration*
ORIGINAL ARTICLE

New York City Panel on Climate Change 2019 Report Chapter 2: New Methods for Assessing Extreme Temperatures, Heavy Downpours, and Drought

Jorge E. González,[1] Lea Ortiz,[1] Brianne K. Smith,[2] Naresh Devineni,[3] Brian Colle,[4] James F. Booth,[5] Arun Ravindranath,[3] Lea Rivera,[3] Radley Horton,[6] Katie Towey,[5] Yochanan Kushnir,[6] Danielle Manley,[7] Daniel Bader,[7] and Cynthia Rosenzweig[8]

[1]Mechanical Engineering Department, NOAA-CREST Center, The City College of New York, New York, New York. [2]Department of Earth and Environmental Science, CUNY-Brooklyn College, New York, New York. [3]Department of Civil Engineering, NOAA-CREST Center, The City College of New York, New York, New York. [4]School of Marine and Atmospheric Sciences, Stony Brook University, Stony Brook, New York. [5]Department of Earth and Atmospheric Sciences, The City College of New York, New York, New York. [6]Lamont-Doherty Earth Observatory, Columbia University, Palisades, New York. [7]Center for Climate Systems Research, Columbia University, New York, New York. [8]NASA Goddard Institute for Space Studies, New York, New York

Keywords: regional climate; extreme events; downscaling; heat waves; inland flooding; water resources

Contents

2.1 Introduction

This New York City Panel on Climate Change (NPCC3) chapter builds on the projections developed by the second New York City Panel on Climate Change (NPCC2) (Horton *et al.*, 2015). It confirms NPCC2 projections as those of record for the City of New York, presents new methodology related to climate extremes, and describes new methods for developing the next generation of climate projections for the New York metropolitan region. These may be used by the City of New York as it continues to develop flexible adaptation pathways to cope with climate change. The main topics of the climate science chapter are:

(1) Comparison of observed temperature and precipitation trends to NPCC2 2015 projections.
(2) New methodology for analysis of historical and future projections of heatwaves, humidity, and cold snaps.
(3) Improved characterization of observed heavy downpours.
(4) Characterization of observed drought using paleoclimate data.
(5) Suggested methods for next-generation climate risk information.

The focus of NPCC3 is on high-risk events involving extreme temperatures, extreme precipitation, and drought. Current trends are presented using historical climate records of high temperature, cold snaps, humidity, and extreme precipitation for the New York metropolitan region. The geographical span of the New York metropolitan region considered here includes, in addition to New York City, adjacent sections of New Jersey such as Newark, Jersey City and Elizabeth, as well as other nearby locations in New York such as Yonkers and Long Island. Historical records of droughts in the Delaware watershed region are also examined. Each climate extreme is analyzed for detection of current trends, and future projections

[Correction added on June 12, 2019, after first online publication: In the author list, the eighth author's name was changed from "Luis Rivera" to "Lea Rivera."]

doi: 10.1111/nyas.14007

are updated for high-temperature extremes as a test of new methods that could be utilized by NPCC4.

These represent finer temporal and spatial resolutions that may be of practical use to key stakeholders in New York City for planning purposes and/or emergency responses. They include local projections of extreme heat and demonstrate the role of the heterogeneous landscape of the city in each process (e.g., how the urban heat island (UHI) affects city neighborhoods differently). Each section of the chapter presents definitions, baselines, methods, and projections, along with uncertainties and recommendations for future work.

2.2 NPCC3 approach

As in NPCC2, NPCC3 makes use of definitions, measurements, baselines, and scenarios to represent how the probabilities of climate events may change in the future. Here, the focus is on extreme events. For most climate hazards, the definitions of extremes are consistent with the NPCC2, specifically for extreme heat, cold spells, and precipitation.

NPCC3 confirms the temperature and precipitation projections of NPCC2 as those of record for use in planning. Based on emerging science, NPCC3 introduces a new methodology for analyzing heat and precipitation extremes that could be used for developing future projections of record in NPCC4.

In NPCC2, temperature analyses included projections of average temperature changes and changes in heat waves and hot days. NPCC3 explores new methodologies for downscaling heat extremes and introduces new metrics to analyze historical and projected humidity. For precipitation, NPCC2 developed quantitative projections for average rainfall and daily maximum rainfall events, and NPCC3 introduces a methodology for quantifying projections for sub-daily heavy downpour rain events.

In addition, NPCC3 examined how current observations of temperature and precipitation changes compare to projected changes from NPCC2 into the 2020s time slice, which encompassed the time period from 2010 to 2039. Figure 2.1 shows the results of this analysis and demonstrates that observations from 2010 to 2017—the period for which both observed data and NPCC2 projections are available to compare—have been largely consistent with projected changes in average conditions for both temperature (Fig. 2.1a) and precipitation (Fig. 2.1b). However, these comparisons should be viewed with caution because of the role that natural variation plays in the short term.

As NPCC3 shifts from a focus on average conditions to extremes, the baselines in some cases vary according to the relevance of the period for the extreme event researched and the period for which data are available. To the extent possible, consistency with NPCC2 is maintained. For example, the baseline for heat waves is 1971–2000, which is the same as NPCC2. However, NPCC3 uses summer months for extreme heat events (June, July, and August) for three reference weather stations, while NPCC2 used the whole year with one reference weather station.

NPCC3 uses bias-corrected statistical downscaling and develops future projections for extreme heat based on summer seasons only and includes high-resolution dynamical downscaling at 1 km for selected time slices. Summer humidity is included in the projections as a new heat-related variable. The section of extreme temperatures closes with a short view of cold spells and winter extremes.

The section on urban flooding makes use of shorter, more detailed records of satellite and radar data to demonstrate the spatial distribution of these extreme events at sub-hourly time resolution.

For droughts, a much longer precipitation record based on tree rings is used to capture decadal variations in the New York City watershed region, and reconstructions of inflows to reservoirs are used to understand how frequently extreme droughts have occurred in the past.

To create the new extreme event projections, bias-corrected statistical downscaling is used (see Section 2.3). In the Appendix, we provide an example of dynamic downscaling, a method that can capture the role of the urban built environment in magnifying heat events and mitigating flooding events.

Model outputs from the fifth phase of the Coupled Model Intercomparison Project (CMIP5; Taylor *et al.*, 2012) are used for projections of extreme heat. Methods for calculating future projections are consistent with NPCC2 but are updated to account for climate model biases in simulating the distribution of temperature (National Climate Assessment; Walsh *et al.*, 2014). Results are provided in 30-year intervals centered on the 2020s, 2050s, and 2080s as defined by NPCC2. The ensemble of CMIP5 results includes two representative concentration pathways (RCPs) (see Box 2.1).

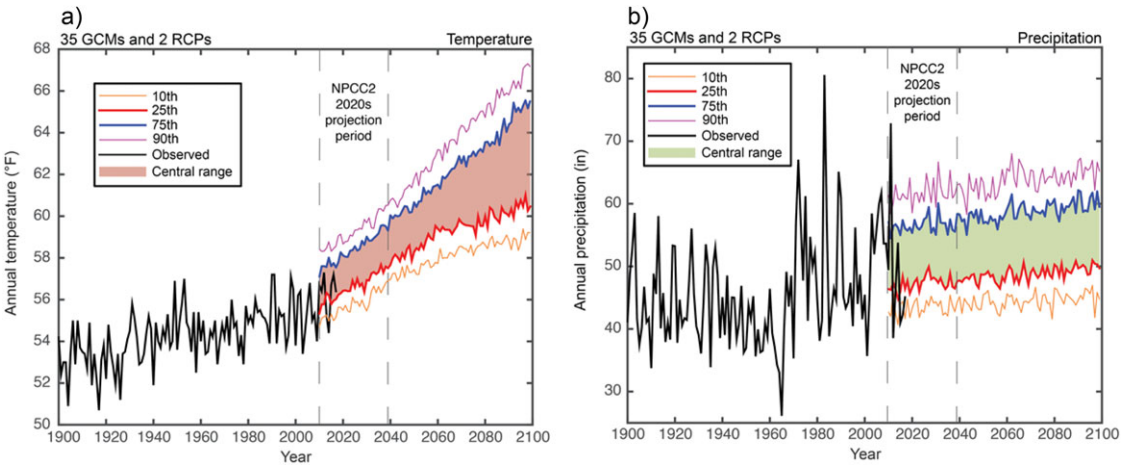

Figure 2.1. Observations at Central Park (1900–2017) compared to the 2020s (2010–2039) time slice of NPCC2 projected changes for (a) average annual temperature and (b) average annual precipitation. Colored lines represent the 10th, 25th, 75th, and 90th percentiles of model projections across RCPs 4.5 and 8.5 for 35 GCMs. Shading shows the central range of projections between the 25th and 75th percentiles. Vertical dotted lines represent the range of the 2020s time slice from 2010 to 2039. Observed data are from the United States Historical Climatology Network (USHCN), and climate projections are from the Coupled Model Intercomparison Project Phase 5 (CMIP5).

Note: These comparisons should be viewed with caution because of the role that natural variation plays in the short term.

2.3. Extreme temperature and humidity

Summer (defined as the months of June, July, and August) temperatures are expected to increase in New York City throughout the 21st century (Horton *et al.*, 2015), leading to more frequent and intense extreme heat events known as heat waves. Here, we follow the definition of heat waves according to the National Weather Service (NWS), that is, an interval of 3 (or more) consecutive days with temperatures of at least 90 °F (32.22 °C).

Heat waves affect a wide range of human activities. These effects include increasing energy demand (Schaeffer *et al.*, 2012; Sailor, 2001; Santamouris, 2014) and mortality (Knowlton *et al.*, 2007; Luber and McGeehin, 2008; Anderson and Bell, 2010; Rosenthal *et al.*, 2014). Moreover, higher temperatures associated with urbanization, a phenomenon called the Urban Heat Island (UHI) (Oke, 1982), exacerbate the impacts of extreme heat events (Li and Bou-Zeid, 2013; Ramamurthy and Bou-Zeid, 2016; Ramamurthy *et al.*, 2017; Ortiz *et al.*, 2018).

New York City, being the most populated urban area in the United States with over 8 million people (U.S. Census Bureau, 2018), has a large human and economic incentive to understand and mitigate the negative impacts of these events now and in the future.

Extreme heat projections have primarily been developed on global (Meehl and Tebaldi, 2004) or continental scales (Gao *et al.*, 2012), with less work focusing on local urban projections that require accounting for finer-scale processes and feedbacks that may affect the occurrence and characteristics of high-temperature events. An example of these processes is the soil moisture-heat wave feedback, wherein dry soil conditions may amplify heat waves by reducing available moisture for evaporative cooling (Seneviratne *et al.*, 2006; Lorenz *et al.*, 2010; Fischer *et al.*, 2007). Cities may amplify these feedbacks by reducing exposed soil area, greatly reducing the capacity for water retention near the land surface (Li and Bou-Zeid, 2013; Ramamurthy and Bou-Zeid, 2016; Ramamurthy *et al.*, 2017).

Other relevant city-scale processes include waste heat from buildings and transportation (Taha, 1997; Ichinose *et al.*, 1999; Offerle *et al.*, 2005), lower surface reflectivity of built surfaces (Taha *et al.*, 1988; Morini *et al.*, 2016; Ramamurthy *et al.*, 2015) and increased heat storage in buildings and built structures (Oke *et al.*, 1981; Arnfield and Grimmond, 1998).

Humidity content of the atmosphere can play an adverse role in how humans react to high heat conditions (Davis *et al.*, 2016; Hass *et al.*, 2016).

As air becomes more saturated with water vapor, the human body becomes less able to shed excess heat through evaporative cooling of perspiration. This can lead to exacerbation of high-temperature impacts such as fatigue and heat exhaustion.

This section presents extreme heat and specific humidity projections for New York City using new methods, accounting where possible for urban effects via statistical processing of global climate model (GCM) simulation data. This statistical processing, or downscaling, is necessary because global models have, in general, very coarse spatial resolution (>100 km^2) and are thus not able to resolve coastlines, topography, and land cover.

The downscaling technique used by NPCC3 is *histogram matching*. It aims to adjust the model representations of observed climate by correcting their *mean* and *variance* to match a representative set of observations in the target domain (see Appendix 2.B). This differs from the bias adjustment procedure of NPCC2 that combined GCM results with station records to downscale the projections to the New York metropolitan region using the "delta method" (Horton *et al.*, 2015), where mean monthly projected changes are applied to daily observations.

In NPCC3, as in NPCC2, the climate projections are based on multiple climate models, driven by two RCPs—RCP4.5 (referred to as medium emissions) and RCP8.5 (referred to as high emissions) (see Box 2.1). The aim of this approach is to capture the uncertainties emerging from the range of model results as well as those related to the impacts of future industrial activity, energy use, and technology on greenhouse gases (GHGs), aerosol emissions, and land use change. For consistency, NPCC3 uses the same baseline period as the NPCC2 (1971–2000). Definitions and methods are detailed in Table 2.1.

Box 2.1. Definitions and terms

Climate change

Climate change refers to a significant change in the state of the climate that can be identified from changes in the average state or the variability of weather and that persists for an extended time period, typically decades to centuries or longer. Climate change can refer to the effects of (1) persistent anthropogenic or human-caused changes in the composition of the atmosphere and/or land use, or (2) natural processes such as volcanic eruptions and Earth's orbital variations (IPCC, 2013).

Global climate models (GCMs)

A GCM is a mathematical representation of the behavior of the Earth's climate system over time that can be used to estimate its sensitivity to atmospheric concentrations of greenhouse gases (GHGs), aerosols, and land use change. Each model simulates physical exchanges among the ocean, atmosphere, land, and ice.

Representative concentration pathways (RCPs)

RCPs are sets of trajectories of concentrations of GHGs, aerosols, and land-use changes developed for climate models as a basis for long-term and near-term climate-modeling experiments (Moss *et al.*, 2010). RCPs describe different climate futures based on different amounts of climate forcings. These data are used as inputs to GCMs to project the effects of these drivers on future climate. The NPCC uses sets of GCM simulations driven by two RCPs, known as 4.5 and 8.5. The set of GCM simulations driven by RCP 4.5 is defined here as a medium-emissions scenario, and that by RCP 8.5 as a high-emissions scenario.

Climate change risk information

On the basis of the selection of the RCPs and GCM simulations, local climate change information is developed for key climate variables—temperature, precipitation, and associated extreme events. These results and projections reflect a range of potential outcomes for the New York metropolitan region.

Climate hazard

A climate hazard is a weather or climate state such as a heat wave, flood, high wind, heavy rain, ice, snow, or drought that can cause harm and damage to people, property, infrastructure, land, and ecosystems. Climate hazards can be expressed in quantified measures, such as flood height in feet, wind speed in miles per hour, and inches of rain, ice, or snowfall that are reached or exceeded in a given period of time.

Uncertainty

Uncertainty denotes a state of incomplete knowledge that results from lack of information, natural variability in the measured phenomenon, instrumental and modeling errors, and/or from disagreement about what is known or knowable (IPCC, 2013).

Table 2.1. Methods for heat extremes used in NPCC2 and NPCC3

Methods	NPCC2 (2015)	NPCC3 (2018)
Definition of heat wave	• Three or more consecutive days at or above 90 °F	• Three or more consecutive days at or above 90 °F
Metrics	• Number of heat waves per year • Duration of heat wave (number of days average heat wave lasts) • Total days at or above 90 °F per year • Total days at or above 100 °F per year	• Number of heat waves per year • Duration of heat wave (number of days average heat wave lasts) • Average maximum temperature during heat wave (heat wave intensity) • Total days above 90 °F per year • Total days above 100 °F per year • Annual mean specific humidity
Baseline years	1971–2000	1971–2000
Baseline reference locations	Central Park	Central Park (extreme heat) LaGuardia Airport (extreme heat, humidity) JFK Airport (extreme heat)
Baseline values	• 2 heat waves per year • 4 days in duration • 18 days at or above 90 °F • 0.4 days at or above 100 °F	• 1.1 heat waves per year • 4 days in duration • 94.2 °F maximum temperature • 9.6 days above 90 °F • 0.27 days above 100 °F • 0.0123 kg_{vapor}/kg_{air} mean specific humidity
Future time slices	• 2020s (2010–2039) • 2050s (2040–2069) • 2080s (2070–2099)	• 2020s (2010–2039) • 2050s (2040–2069) • 2080s (2070–2099)
Methodology	• 2 RCPs (4.5 and 8.5) • 35 GCMs • 10th, 25th, 75th, and 90th percentiles[c] across both RCPs and 35 GCM outputs • Delta method used for GCM bias correction	• 2 RCPs (4.5 and 8.5) • 26[a] GCMs • 10th, 25th, 75th, and 90th percentiles across both RCPs and 26 GCM outputs • GCM mean and variance bias correction to temperature station records[b].

[a]NPCC3 uses a smaller GCM ensemble than the 35-model ensemble used in NPCC2 because not all GCMs provide specific humidity as a standard output.
[b]Bias correction is performed on GCM data in order to improve how representative a single grid box is to local New York City conditions.
[c]The Xth percentile is defined as the value that X percent of the outcomes are the same or lower than.

2.3.1 Observed trends in summer heat waves

Historical trends of daily maximum summer temperature in New York were analyzed using Central Park weather station, John F. Kennedy (JFK), and LaGuardia Airports during June, July, and August (Fig. 2.2). Central Park has the longest historical record, dating back to 1900, where the average annual daily maximum summer temperature has been rising at an average of 0.2 °F per decade from 1900 to 2013. JFK and LaGuardia weather stations go back to 1970, where average annual daily maximum summer temperatures have been increasing at a rate of 0.5 °F per decade and 0.7 °F per decade, respectively.

The distance between these weather stations provide insights into processes that affect temperatures near the surface, such as sea breezes[a] and the UHI. Sea breeze effects appear in stations located close to Long Island's southern shore (e.g., JFK), with lower

[a]Sea breezes form due to temperature differences between the air over land and ocean and are a feature of New York City coastal areas (Haurwitz, 1947; Childs and Raman, 2005).

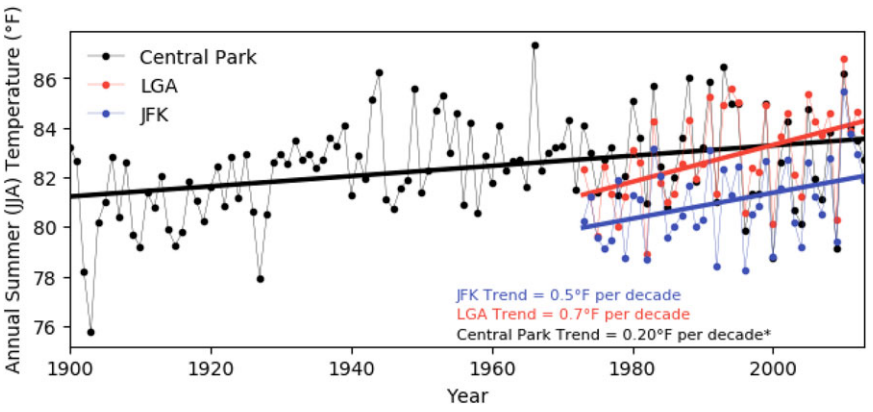

Figure 2.2. Annual average daily maximum summer temperatures. (June, July, August) in Central Park from 1900 to 2013, LaGuardia (LGA) airport from 1970 to 2013, and John F. Kennedy (JFK) airport from 1970 to 2013. Solid lines represent linear trends for each station. Station records were obtained from the U.S. Historical Climatology Network (USHCN) Version 2.5 (Menne *et al.*, 2013). *Central Park trend is significant at 0.01 level, while LGA and JFK trends are positive but not significant, possibly due to shorter record length.

daily maximum temperatures compared to their in-land counterparts (Fig. 2.2).

Sea breeze impacts on temperatures show that geospatial heterogeneity of the urban landscape plays a role in near-surface temperatures, and therefore impact occurrences of extreme heat. The weather station located at JFK, which experiences afternoon sea breezes, has a mean summer maximum temperature of 80.6 °F, whereas the other stations have a mean value of 82.7 °F, which is 2.1 °F higher. This is consistent with climatological studies (e.g., Gedzelman *et al.*, 2003) of the UHI in the region, which have found that afternoon summer sea breezes may shift the center of the urban heat island west and north, toward New Jersey and The Bronx.

2.3.2 New methods for projected changes in heat waves

This section describes new methods and results for NPCC3 projected changes in heat waves. Projections are presented in two formats:

- Graphical time series: Results shown as a time series are further broken out into the two RCP scenarios used in NPCC3 (see Fig. 2.3). These include a medium-emissions scenario (RCP4.5) (Thomson *et al.*, 2011) and a high-emissions scenario (RCP8.5) (Riahi *et al.*, 2011).
- Time slices table: Results are summarized for the 10th, 25th, 75th, and 90th percentile of climate model outcomes across both RCP 4.5 and 8.5 scenarios in Table 2.2, averaged by 30-year time slices centered around the 2020s (2010–2039), 2050s (2040–2069), and 2080s (2070–2099) decades.

2.3.2.1 Heat wave frequency, duration, and intensity. Heat wave characteristics considered here are their frequency (events/year), mean event duration (number of days/event), and intensity (average maximum temperature/heat wave). NPCC2 had previously analyzed frequency and mean event duration; heat wave intensity is a new metric in NPCC3. While a new methodology is tested here that is different from NPCC2, NPCC3 confirms the use of NPCC2 projections as the projections of record for New York City to plan for extreme heat. The new methodologies presented in NPCC3 could be used in developing new projections of record in NPCC4.

Using a composite observed temperature record derived by averaging the daily maximum temperature over the three New York City stations, results from 26 GCMs were bias corrected in order to project distributions of heat waves for the NPCC3 time slices following the methods of Piani *et al.* (2010) and Hawkins *et al.* (2013). (See Appendix 2.C for detailed methods.) The mean and standard deviation of a given variable were used to adjust the model distribution against the target observed distribution. For each GCM, the closest

Table 2.2. Results from new projection methods for future assessments of heat wave across 52-member ensemble (26 models, RCPs 4.5 and 8.5) for New York City

		10th percentile	25th percentile	75th percentile	90th percentile
Heat waves per year (average number of events per year)	2020s	1	2	4	5
	2050s	2	3	5	6
Baseline[a] 1.1	2080s	2	3	5	7
Mean heat wave duration (average heat wave length in days)	2020s	3	4	6	8
	2050s	4	5	9	13
Baseline 4	2080s	4	6	15	27
Mean heat wave intensity (average maximum temperature during heat wave event in °F)	2020s	91.8	92.5	94.5	95.7
	2050s	92.6	93.5	95.4	96.5
Baseline 94.2 °F	2080s	93.2	94.2	97.1	99.1
Days above 90 °F (average number of days per year)	2020s	6	11	25	34
	2050s	15	24	46	56
Baseline 9.6	2080s	24	35	63	75
Days above 100 °F (average number of days per year)	2020s	0	0	0	2
	2050s	0	0	4	8
Baseline 0.27	2080s	0	1	13	27

[a]Baseline refers to 1971–2000 average characteristics for Central Park, LaGuardia, and JFK.

Note: NPCC3 confirms the temperature projections of NPCC2 as those of record that should be used for planning.

land grid point was selected, as was done in NPCC2, and the distribution of maximum daily temperature at this point was bias corrected against the city's composite maximum temperatures. This method is referred to as a "single-point" bias correction.

The previous NPCC2 approach may have resulted in a bias toward slightly cooler projected extreme temperatures compared to those projected using the NPCC3 bias-correction methods, particularly toward the warmer periods in the 2080s time slice. These changes may be due to the correction to the variance that, at least partially, addresses the fact that GCM grid boxes near coasts may include water.

NPCC3 analysis of the bias-corrected single-point projections shows overall increase across all heat wave metrics throughout the 21st century (Fig. 2.3). To highlight the sensitivity to emission scenarios, we present the response to medium-emission and high-emission scenarios separately. In Table 2.2, the projections are based on the distribution of multimodel results showing the 10th, 25th, 75th, and 90th percentile outcomes across both RCP scenarios, as was done in NPCC2.

Mean daily maximum temperature (Fig. 2.3a) shows a nearly linear trend in the high-emissions scenario (RCP8.5), whereas the rate of change in the medium-emissions scenario (RCP4.5) slows after 2040.

The number of heat waves per year (Fig. 2.3b) shows far less deviation between the two emissions scenarios. Both scenarios increase at a pace of about one additional yearly event every 20 years until 2060, where growth slows down considerably. This may be due to consecutive events coalescing into very long heat waves, which becomes more likely as heat waves increase in length and frequency. It is also an artifact of the definition of heat wave used, which establishes an unchanging temperature threshold through the entire century. As mean temperatures increase, meeting the 90 °F on consecutive days becomes more likely. Uncertainty in projections as described by confidence intervals increase over time, with a spread of 1 event in the first half of the century that grows to a spread of about two events by end of century.

Mean event duration projections (Fig. 2.3c) are similar across the scenarios in the first half of the century, growing by around 2 days per 20-year period. However, the high-emissions scenario projections show accelerated growth in the latter half of the century, as well as more spread in the model ensemble, with an uncertainty band spanning about 10 days, compared to about 2 days

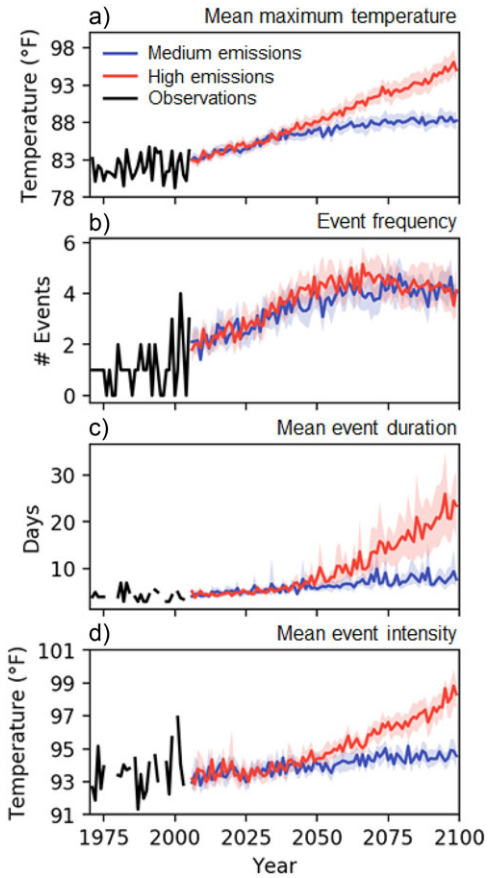

Figure 2.3. Results from new bias-corrected projections for future assessments of (a) mean daily maximum temperature, (b) event frequency, (c) mean event duration, and (d) mean event intensity compared to the 1971–2000 base period. Solid lines represent the multimodel mean of a 26 global climate model ensemble, while shaded bands show 95% confidence intervals. Black lines indicate observations from three GHCN stations—Central Park, JFK, and LaGuardia—between 1971 and 2000.

in the first half. This accelerated increase in event duration may explain the stabilization of event frequency projections in Figure 2.3(b), as events may aggregate into longer heat waves.

Mean intensity, defined as the mean of event maximum temperatures, shows large interannual variation (Fig. 2.3d), with projected values that increase from about 93 °F early in the century, to 95–98 °F by the end of the century. Confidence interval bands increase slightly throughout by end of century, reaching an ensemble spread of about 1 °F.

2.3.2.2 New methods for warm day analyses.

Additional key metrics of extreme heat explored are number of days above 90 and 100 °F in the summer season (Table 2.2). Projected days above 90 °F are expected to become more likely as summer temperatures increase. By the 2080s, projections show 24 (10th percentile) to 75 (90th percentile) days above 90 °F compared to the 1971–2000 baseline (10 days).[b]

2.3.3 Methods for assessing trends in humidity

The humidity content of the atmosphere can play an adverse role in how humans react to high heat conditions (Davis *et al.*, 2016; Hass *et al.*, 2016). We present projections of daily mean specific humidity based on a 26 multimodel ensemble, across medium- and high-emissions scenarios, as in Section 2.3.2. For each model, the land grid point closest to New York City is used. Due to a lack of specific humidity records from all weather stations, GCM humidity was bias corrected based on LaGuardia Airport only. In addition, the 1971–2000 baseline for specific humidity is based only on the LaGuardia Airport weather station. Humidity is a new metric being considered by the NPCC3.

Results show an increase between the 2020s and 2080s time slices of around 9% at each period's 10th percentile, while changes in the 90th percentile represent a 16% increase (Table 2.3). The uncertainty in these projections as characterized by the model ensemble 95% confidence bands (Fig. 2.4) is relatively large. Increases in specific humidity combined with increasing temperatures might lead to higher heat index (see Box 2.2), which has major consequences for human health and is a driver of peak energy demand for space cooling, as air conditioning systems remove sensible (temperature-related) and latent (moisture-related) heat from buildings. To assess combined air moisture and temperature impacts, concurrent hourly values must be used, rather than daily outputs from the model ensemble.

[b]Although warm days can occur outside of the traditional summer months, here we only consider June, July, and August, as extreme heat days are more likely to occur during this period.

Table 2.3. Specific humidity projections across the 52-member ensemble (26 models, RCPs 4.5 and 8.5) for New York City

		Baseline	10th percentile	25th percentile	75th percentile	90th percentile
Mean specific humidity (kg_{vapor}/kg_{air})	2020s	0.0123	0.0115	0.0119	0.0127	0.0131
	2050s	0.0123	0.0122	0.0126	0.0138	0.0146
	2080s	0.0123	0.0125	0.0130	0.0149	0.0164

Note: Baseline period for humidity is 1971–2000 at the LaGuardia Airport weather station.

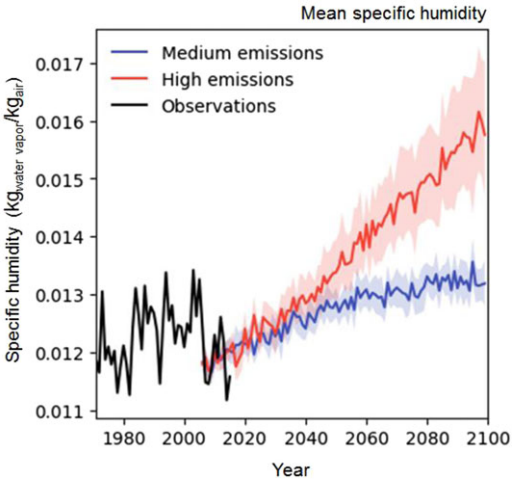

Figure 2.4. Specific humidity projections from the bias-corrected 26-member global climate model ensemble and across the medium (RCP4.5) and high (RCP8.5) emissions scenarios compared to the 1971–2000 baseline period at the LaGuardia Airport weather station. Shaded bands represent 95% confidence intervals across the ensemble. Specific humidity refers to the amount of water vapor in the atmosphere and combined with increasing temperatures can lead to a higher heat index.

Box 2.2. Key humidity definitions

Specific humidity: A measure of the amount of water in the atmosphere; the mass fraction of water vapor per unit mass of moist air.
Absolute humidity: Mass of air per unit volume of moist air.
Relative humidity: The ratio of water vapor pressure to the saturation vapor pressure. It measures how saturated with water vapor the atmosphere is. As air becomes more saturated with water vapor, it becomes more difficult for the human body to shed excess heat through evaporative cooling of perspiration.
Heat index: A measure of the combined effects of temperature and relative humidity. It is defined by the National Weather Service.

See Appendix 2.C of this chapter for an expanded discussion of how climate change is projected to impact the heat index. NPCC3 recommends further testing of this methodology for the development of new projections of record in NPCC4.

2.3.4 Cold snaps

NPCC3 confirms the analysis of NPCC2 days with minimum temperatures below 32 °F as the projections of record for New York City planning. NPCC3 further examines historical extreme cold events, using two measures of extreme cold (Boyle, 1986; de Vries *et al.*, 2012; Chen *et al.*, 2013; Peterson *et al.*, 2008; Efthymiadis *et al.*, 2011):

- A *day below freezing* occurs whenever minimum temperature is equal to or less than 32 °F
- A *cold day* occurs whenever its minimum temperature is equal to or less than the 10th percentile of daily minimum temperature of a given year.

Other definitions vary, including the use of standard deviations (Vavrus *et al.*, 2006). Cold spell changes have been reported on regional scales (e.g., Europe, de Vries *et al.*, 2012; China, Zhang *et al.*, 2017; Northeast United States, Thibeault and Seth, 2014) and for global scales (Vavrus *et al.*, 2006; Konrad, 1996) using GCM ensembles and long-term climate records. In most cases, cold days have shown decreases, and notably in Northern latitudes, it has been found that accelerated decreases of cold spells outpace increases in summer maxima (Thibeault and Seth, 2014).

We used data from Central Park to establish a benchmark for cold spells. The 10th percentile threshold for cold days at this station was computed from the entire 1900–2017 record, with a value of 24.08 °F. In general, cold days per year decreased

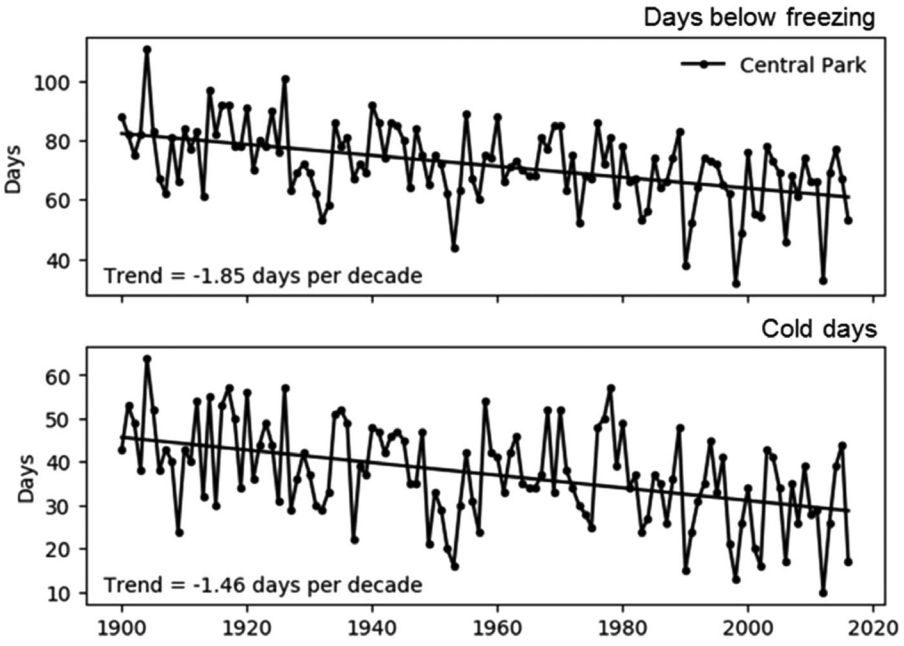

Figure 2.5. **Observed annual number of cold days at Central Park Station (1900–2017). Solid straight lines represent the linear trend in days below freezing temperatures (top) and cold days (bottom). A day below freezing occurs whenever minimum temperature is equal to or less than 32 °F. A cold day occurs whenever its minimum temperature is equal to or less than the 10th percentile of daily minimum temperature of a given year. Station records obtained from the U.S. Historical Climatology Network (USHCN). Both trends are significant at the 0.001 level.**

by 1.46 days every decade between 1900 and 2017, while days below freezing temperatures decreased at a rate of 1.85 days per decade (Fig. 2.5). This results in recent years having, on average, about 22 fewer days below freezing and 17 fewer cold days than in 1900. The rate of change of these trends is slightly lower than those reported for the entire Northeast by Thibeault and Seth (2014).

For the case of New York City, the attribution of these rapid decreases of cold spells may be a combined effect of global warming and urbanization. Urbanization leads to the UHI effect, which tends to have a larger effect in the winter.

2.3.5 Polar vortex and extreme cold events

The impact of global warming on climate implies an overall decrease in the number of cold extremes, while the number of warm extremes increases (Horton *et al.*, 2015). However, recent persistent winter events of record cold weather in the Northeast United States and in other Northern Hemisphere regions raise concern of a possible connection to climate change.

Both the science community (Screen *et al.*, 2015) as well as the public (Lyons *et al.*, 2018) have been engaged in research and discussion about cold air outbreaks associated with the Polar Vortex. An aspect of these discussions is the connection between the gradual disappearance of Arctic sea ice due to the polar amplification of global warming, the increase in atmospheric "blocking" events, and the slowing down and deepening of the wavy circulation in the midlatitudes (Screen and Simmonds, 2010; Overland *et al.*, 2015). With the increase in amplitude and slowdown of atmospheric waves, cold air can flow down from the Arctic deep into the midlatitudes, and *vice versa*, warm air flows north. This creates protracted deviations from normal conditions in either place.

In early January of 2014, a large cold air mass moved from Canada into the northern Great Plains states and made its way slowly to the Northeast. The unusual cold weather in the eastern half of the United States did not abate until April. At the same time, other areas in the Northern Hemisphere experienced record warm winter weather.

Shorter events similar to this have happened since, as was the case during winter months in 2017–2018 and 2019. These events were connected to stratospheric warming, where the low-pressure vortex that is usually centered on the North Pole moves equatorward. This change in circulation is communicated down to the troposphere and results in anomalous weather situations during the winter season (Kretschmer *et al.*, 2018; Screen *et al.*, 2018).

There has been much debate whether such events are linked to the gradual melting of sea ice in the Arctic, and it appears that the answer is that there is a link (Overland *et al.*, 2015; Screen *et al.*, 2018). This was shown in climate models (Zhang *et al.*, 2018) and is consistent with the observation that polar vortex events are on the rise (Kretschmer *et al.*, 2018).

There is, however, no evidence that cold air outbreaks in the United States have increased as a result of this or other phenomena (Screen *et al.*, 2015). The increase in polar vortex events was found to influence surface weather in Siberia, where a significant cooling of the average winter weather has been detected, in contrast with the observed warming elsewhere around the globe (Kretschmer *et al.*, 2018; Zhang *et al.*, 2018).

2.3.6 Summary and future research directions for extreme temperature and humidity

New methodologies for projections of heat wave characteristics for the New York metropolitan region were tested in NPCC3 using bias-corrected climate model projections. For the early part of the century (2020s), these results are consistent with those of NPCC2. In the later part of the century (2050s and 2080s), the NPCC3 results display the potential for more intense heat events with longer durations.

Results show large changes across all heat wave metrics throughout the 21st century. The high-emissions scenario (RCP8.5) projects, in many cases, several times larger effects than the medium-emissions scenario. The uncertainty of the projections increases through time.

The new NPCC3 methods include humidity, which is projected to increase by more than 30% from baseline values. These increases in atmospheric humidity with extreme temperatures are likely to have large societal implications reflected in public health and energy demands.

NPCC3 confirms the NPCC2 projections for heat waves, hot days, and cold days as those of record for New York City in planning for the impacts of climate change and recommends the incorporation of the new methodologies into revised projections of record in NPCC4.

Future work in projecting extreme heat and humidity for the NPCC should be directed to incorporating the spatial distribution of these extreme heat events to account for coastal influence and UHI effects (e.g., sea breeze effects). This may require using regional climate models (RCMs) to dynamically downscale projections to finer spatial scales within the New York metropolitan region. Carrying this out for an ensemble of GCMs and RCMs will require large computational efforts. New methods may be needed to account for uncertainties in dynamic downscaling. See Appendix 2.C for an example of the possible approach, utilizing one GCM and one RCM for two time slices, as a potential guide for new research directions in NPCC4.

2.4 Heavy downpours and urban flooding

NPCC2 projected quantitative changes in daily extreme rainfall amounts for 1 inch, 2 inches, and 4 inches (Table 2.4). NPCC2 also included a qualitative projection in relation to extreme rainfall, stating that heavy downpours in the New York metropolitan region are very likely to increase by the 2080s (Horton *et al.*, 2015).

NPCC3 does not provide new projections for heavy rainfall and confirms the NPCC2 projections as those of record for city planning and adaptation. It provides new analyses of the dynamics of heavy rainfall events in the New York metropolitan region recommended for use in developing new projections of record in NPCC4.

NPCC3 focuses on observed annual rainfall (see Section 2.2) and observed heavy rainfall days in recent years compared to the NPCC2 2020s time slice projections. NPCC3 also analyzes the types of storm systems associated with heavy rainfall events, and the regional drivers of historical flash flooding events. This section also conducts a trend analysis of sub-daily heavy precipitation events at the 1-, 3-, 6-, and 24-h duration. Finally, this section explores ways to illustrate the spatial variation of urban flooding events. It is recommended that this work serve as a foundation for new projections of record

Table 2.4. NPCC2 projected changes in heavy rainfall days (Horton *et al.*, 2015)[a]

Heavy rainfall days	Baseline (1971–2000)	Low estimate (10th percentile)	Middle range (25th to 75th percentile)	High estimate (90th percentile)
2020s				
Number of days rainfall ≥1 inch	13	13	14–15	16
Number of days rainfall ≥2 inches	3	3	3–4	5
Number of days rainfall ≥4 inches	0.3	0.2	0.3–0.4	0.5
2050s				
Number of days rainfall ≥1 inch	13	13	14–16	17
Number of days rainfall ≥2 inches	3	3	4–4	5
Number of days rainfall ≥4 inches	0.3	0.3	0.3–0.4	0.5
2080s				
Number of days rainfall ≥1 inch	13	14	15–17	18
Number of days rainfall ≥2 inches	3	3	4–5	5
Number of days rainfall ≥4 inches	0.3	0.2	0.3–0.5	0.7

[a]Projections are based on 35 GCMs and two RCPs. Baseline data are for the 1971–2000 base period. Projections show the low estimate (10th percentile), middle range (25th–75th percentile), and high estimate (90th percentile) 30-year mean values from model-based outcomes.

Note: NPCC3 confirms the use of these NPCC2 projections as those of record for city policy and planning purposes.

for heavy rainfall that are to be developed in NPCC4.

NPCC3 analyses of heavy downpours build on NPCC2 projections for daily extreme rainfall by more closely examining the past and present rainfall across New York City and across timescales. Additionally, NPCC3 includes observations of urban flooding (definition in Table 2.5), in New York City and surrounding areas. NPCC3 refocuses discussion from daily extreme rainfall to sub-daily "heavy downpours," defined as rarely occurring rainfall at less than daily timescales that can produce urban flooding. NPCC3 lays the groundwork for a new set of future projections in NPCC4 using these metrics.

Extreme rainfall is defined as a rainfall amount that is a rare event, that is, one that approaches the end of the probability distribution of all events. In NPCC2, daily extreme rainfall in the current climate was represented by the number of occurrences of rainfall above 1 inch, 2 inches, or 4 inches per day at the Central Park weather station in New York City.

Extreme rainfall measured at Central Park has significant year-to-year variation such that no statistically significant trends in extreme rainfall can be identified (Horton *et al.*, 2015). (A statistically significant trend indicates that this trend in extreme rainfall would be unlikely to occur by chance). NPCC2 did note that the heaviest 1% of daily rainfalls have increased by approximately 70% between 1958 and 2011 in the Northeast (Horton *et al.*, 2015). NPCC2 used the observed measurements as a baseline (Horton *et al.*, 2015) for projections of extreme rainfall (Table 2.6; Horton *et al.*, 2015).

2.4.1 Extreme rainfall and heavy downpours

This section focuses on extreme rainfall by describing the approaches to heavy downpours in NPCC2 and NPCC3, studying regional drivers of daily and sub-daily heavy rainfall, providing a revised historical analysis of heavy rainfall across New York City, and summarizing new research projecting future changes in heavy downpours in the region.

2.4.1.1 Extreme daily rainfall and links to tropical and extratropical cyclones. NPCC2 results included projections for extreme rainfall in the 2020s (2010–2039), 2050s (2040-2069), and 2080s (2070–2099) compared to the baseline (1971–2000) at Central Park. Data for the first 8 years of the 2020s time slice can now be compared to projections—as has been done above with climate averages in Section 2.2. However, several caveats should be kept in mind. First, the fewer years of data, the more likely that year-to-year variations will outweigh any longer-term climatic trends in data. Second, if there is a substantial climatic trend in rainfall extremes, the first 8 years of a 30-year

Table 2.5. NPCC3 rainfall and urban flooding definitions

Term	Definition
Daily extreme rainfall	Rainfall depths at the high end of the rainfall probability distribution; defined as the number of days per year that exceed 1 inch, 2 inches, and 4 inches of rainfall averaged across New York City
Heavy downpours	Rainfall at 1-, 3-, 6-, and 24-h durations that may cause urban flooding; for statistical analyses, annual maximum values are used heavy rainfall intensities may differ across New York City rain gauges.
Days of known flooding	Urban flooding identified by experts (emergency managers and National Weather Service) through either New York City Hazard Mitigation Reports or the National Centers for Environmental Information (NCEI) Storm Events Database.
Urban flooding	Surface flooding of an urban (generally over 20% impervious) area. Urban flooding is caused by rain falling faster than local conveyance systems (sewers or streams) can transmit it. When available, streamflow data from small urban streams in the New York City metropolitan region are used as a proxy for New York City urban flooding data sets.

time slice may look substantially different than the last 8 years of the time slice.

Table 2.7 shows the 2020s (defined as 2010–2039) extreme daily rainfall projections from NPCC2 compared to actual rainfall data from 2011 to 2017 and the baseline values from 1970 to 2003. The first observed 8 years of the 2020s time slice show that observed heavy daily rainfall totals have fallen within the low- to middle-range estimate of the projected amounts.

NPCC3 provides supplemental information by conducting a benchmark analysis on the seasonal characteristics governing daily precipitation extremes in the recent historical record, as well as an overview of recent studies of precipitation extremes that have occurred since NPCC2.

The primary large weather systems that affect New York City are cyclones. Cyclones refer to low-pressure regions where air converges and causes uplift. Cyclones can include extratropical cyclones, caused by mid-latitude weather fronts (e.g., Nor'Easters) and tropical cyclones, which originate in the tropical oceans (e.g., hurricanes). The tracks for both types of cyclones are used to associate extreme precipitation with storms.

The precipitation data used in this section are daily weather station data from JFK, LaGuardia, and Newark International Airports available from the Integrated Surface Database (Smith *et al.*, 2011). The

Table 2.6. NPCC2 daily extreme rainfall analyses (from Horton *et al.*, 2015)

Extreme precipitation methods	NPCC2 (2015)
Definitions	• Individual days per year with rainfall at or above 1 inch • Individual days per year with rainfall at or above 2 inches • Individual days per year with rainfall at or above 4 inches
Metric	• Number of days per year with rainfall reaching at or above daily rainfall total
Baseline years	1971–2000
Baseline values	• 13 days (1 inch) • 3 days (2 inches) • 0.3 days (4 inches)
Future time slices	30-year time slices for • 2020s (2010–2039) • 2050s (2040–2069) • 2080s (2070–2099)
Methodology	• 2 RCPs (4.5 and 8.5) • 35 GCMs • 10th, 25th, 75th, and 90th percentiles across both RCPs and 35 GCM outputs

Table 2.7. Comparison of NPCC2 daily extreme rainfall projections for the 2020s time slice (2010–2039) to observed values at Central Park (2011–2017) and baseline values (1971–2000)

Heavy rainfall days	Baseline values (1971–2000)	NPCC2 2020s low estimate (10th percentile)	NPCC2 2020s middle range (25th–75th percentile)	NPCC2 2020s high estimate (90th percentile)	Observed values (2011–2017)
Number of days ≥1 inch	13	13	14–15	16	14.1
Number of days ≥2 inches	3	3	3–4	5	2.7
Number of days ≥4 inches	0.3	0.2	0.3–0.4	0.5	0.4

Note: These comparisons should be viewed with caution because of the role that natural variation plays in the short term.

extremes are defined as 24-h precipitation for the top 1% of days for the record, per station, which translates to 138 days per site. The baseline period used, 1979–2016, was selected based on the availability of satellite-era gridded sea-level pressure (SLP) reanalysis data (Dee *et al.*, 2011). SLP fields are used to track extratropical cyclone centers via the numerical algorithm of Bauer *et al.* (2016). Cyclone association is calculated by checking if a cyclone center is within 1000 km of New York City on the date of the precipitation event. However, all cyclones that ended up being associated with a precipitation extreme passed within 500 km of New York City. Additional details of the analysis method are in Towey *et al.* (2018).

Daily (24-h) precipitation extremes during the 1979–2016 period occurred most often in August, but more than one event occurred in each month of the year. For events in winter months, the precipitation more likely fell as snow, but the snow water equivalent is used for this analysis.

Figure 2.6 summarizes the annual cycle for extreme 24-h precipitation events. Extratropical

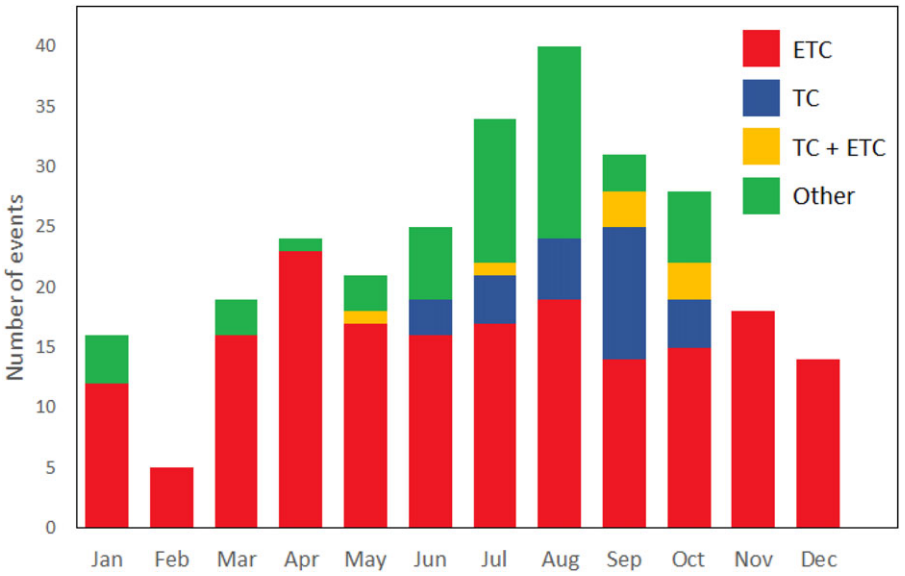

Figure 2.6. Total number of extreme 24-h precipitation events at three New York metropolitan region airports (JFK, LaGuardia, and Newark) per month from 1979 to 2016 correlated with storm type. If more than one airport measured a precipitation extreme on the same date, then that event is only counted once in this figure. ETC refers to extra-tropical cyclones and TC to tropical cyclones; TC + ETC are hybrid storms that display characteristics of both types. Cyclones are identified using Modeling, Analysis, and Prediction (MAP) Climatology of Midlatitude Storm Area (MCMS; Bauer *et al.*, 2016). Tropical cyclones are distinguished by the presence of HURicane DATabase tracks. "Other" refers to high precipitation events differing from tropical and extratropical cyclones that may be related to small-scale storms.

cyclones cause the largest number of extreme 24-h precipitation events in each month of the year. Tropical cyclone and non-cyclone events tend to occur in summer and early fall. Other events may simply be related to small-scale storms. These types of storms are likely to drop all their precipitation in a short time period and be associated with shorter-term heavy rainfall. They are the focus of the remainder of this section. For a more detailed analysis of extreme rainfall and cyclones, see Appendix 2.D.

2.4.1.2 Regional outlook on heavy rainfall at sub-daily scales. Building upon the daily rainfall extremes analysis in NPCC2, NPCC3 also reviews methods to examine heavy downpours that often drive urban flooding, with analysis of sub-daily events occurring at 1- to 6-h timescales (Smith *et al.*, 2013). Rainfall that drives urban and flash flooding in the Northeast is typically temporally and spatially concentrated and is most often caused by thunderstorms (Fig. 2.7; Smith and Smith, 2015).

Regarding projections, NPCC2 included a qualitative projection that downpours are "very likely" to increase by the 2080s. NPCC3 does not update this prediction but does establish heavy downpours as an additional quantitative variable to be included in projections in NPCC4.

Since NPCC2 there have been a few new studies using GCM projections of precipitation extremes in the Northeast United States. The results from these studies are consistent with the NPCC2 Report in that they project an increase in precipitation, both in terms of the mean and extremes for the region (Ning *et al.*, 2015). These precipitation changes are expected to occur in both winter and summer seasons (Fan *et al.*, 2014).

However, the uncertainty in these precipitation projections is much larger than the uncertainty in the modeled temperature projections. One reason for the uncertainty is the presence of modes of natural variability, such as the North Atlantic Oscillation,[c] that affect precipitation in the New York metropolitan region. These can have strong interannual impacts on the location and the types of cyclones that generate at least half of the strong precipitation events for the region (see, e.g., Hall and Booth, 2017). Additionally, the issue of characterizing and projecting Northeast U.S. precipitation extremes and their relationship to natural climate variability has been found to be more complicated than understanding the cyclone tracks (Ning and Bradley, 2014).

Recent studies have projected future rainfall intensity–duration–frequency (IDF) curves for New York State. These project future rainfall extremes for durations longer than 1 h using a set of downscaled GCMs and RCMs (Castellano and DeGaetano, 2015; DeGaetano and Castellano, 2017; Castellano and DeGaetano, 2017). Future IDF curves were developed by using change factors calculated as change in rainfall between past observations and downscaled climate model projections of future rainfall. These projections, which can be found online at http://ny-idf-projections.nrcc.cornell.edu/, are more certain for rainfall durations of more than 24-h than for those under 24 hours. These are peer-reviewed, local, sub-daily rainfall projections available for New York City, used in development of the New York City Climate Resiliency Design Guidelines (http://www.nyc.gov/resiliency).

2.4.1.3 Heavy downpours: past trends and baselines. For NPCC3, historical trends in heavy downpours were analyzed using hourly data from multiple New York City area NOAA rain gauges at Central Park, LaGuardia Airport, JFK Airport, and Newark Airport. This analysis allows for an investigation of trends in short-duration heavy downpours. Heavy downpours, defined as the annual maximum hourly, 3-hourly, 6-hourly, and daily rainfall depths were analyzed for change points. Change points indicate that the median rainfall depth has significantly changed in that year, while trends indicate a gradual and continuous shift in medians throughout the time-period (see Fig. 2.8 for examples). Methods for determining trends in extreme rainfall included the nonparametric Pettitt Test (Pettitt, 1979), nonparametric Mann-Kendall Test (Mann, 1945; Kendall, 1975), and Sen's Slope (Sen, 1968).

Historic trends in heavy downpours are difficult to establish. The natural annual variation in rainfall maxima is generally more significant than trends over time, so that few statistically significant change

[c] The North Atlantic Oscillation, or NAO, is a fluctuation in sea-level atmospheric pressure between the Icelandic Low and Azores High. It influences climate patterns in the Northern Hemisphere.

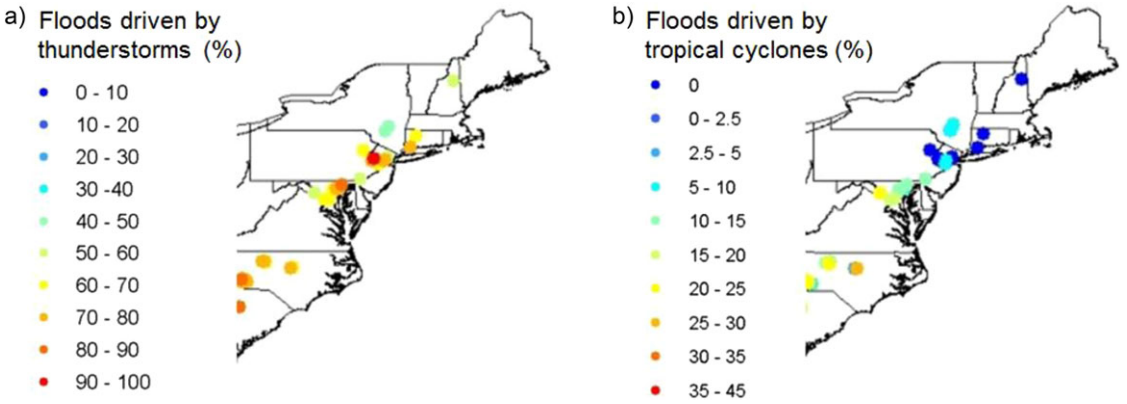

Figure 2.7. Proportion of recent flash flood events (streamflow $>92\ ft^3/s/mi^2$ or $1\ m^3/s/km^2$) on small ($<5.8\ mi^2$ or $15\ km^2$) USGS gauged streams in the Northeastern United States caused by (A) thunderstorms and (B) tropical cyclones. (Adapted from Smith and Smith, 2015). Thunderstorms are distinguished by the presence of lightning flashes, while tropical cyclones are distinguished by the presence of HURicane DATabase tracks. Data are for the entire period of record for each stream gauge, generally from the mid-1980s to 2015.

points or trends can be found in the rainfall record (see Appendix 2.D for specific results).

Statistical results indicate that change points can be detected at the Central Park rain gauge in the mid-1960s at the 3- to 24-h timescale for annual maximum rainfall. Change points can also be detected at the Newark Airport rain gauge in 1971 for 1- and 24-h annual maximum rainfall. These change points may represent a meteorological regime shift associated with the wetter years after the mid-1960s drought, or they may represent changes in recording. After accounting for change points, few rainfall records exhibit statistically significant trends in annual maxima. The only significant trend is for the 3-h annual maximum rainfall depth at the JFK Airport rain gauge (Fig. 2.8). Across rain gauges and timescales, it appears that there may have been an upward shift in extreme rainfall in the late 1960s to early 1970s, but that there has been no consistent trend in heavy downpours across the city.

In order to define current baseline and spatial variation for heavy downpours in New York City,

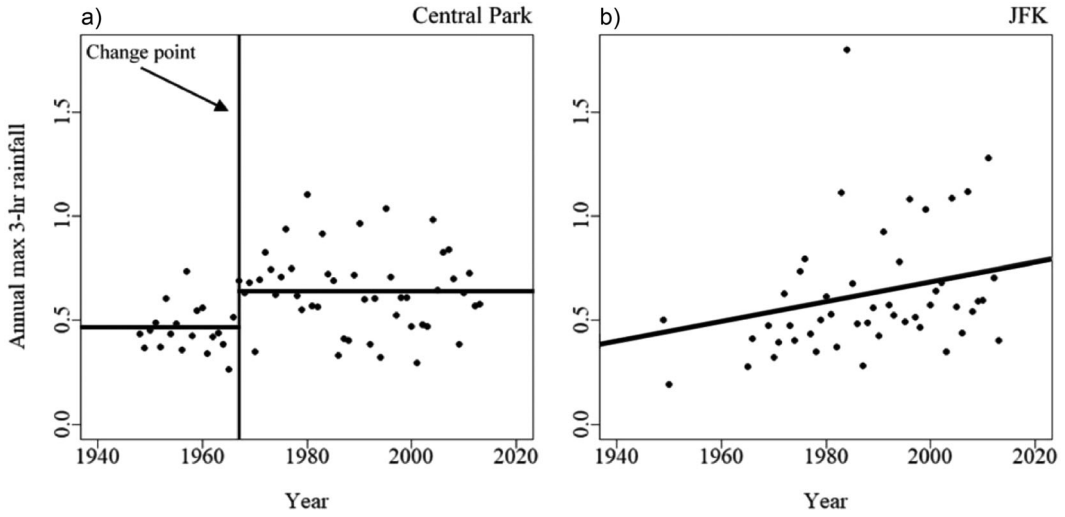

Figure 2.8. Annual maximum 3-h rainfall (in) at Central Park (a) and JFK (b) rain gauges. Central Park displays a change point, a change in median rainfall depth, in 1967 (vertical line), and JFK displays an increasing trend.

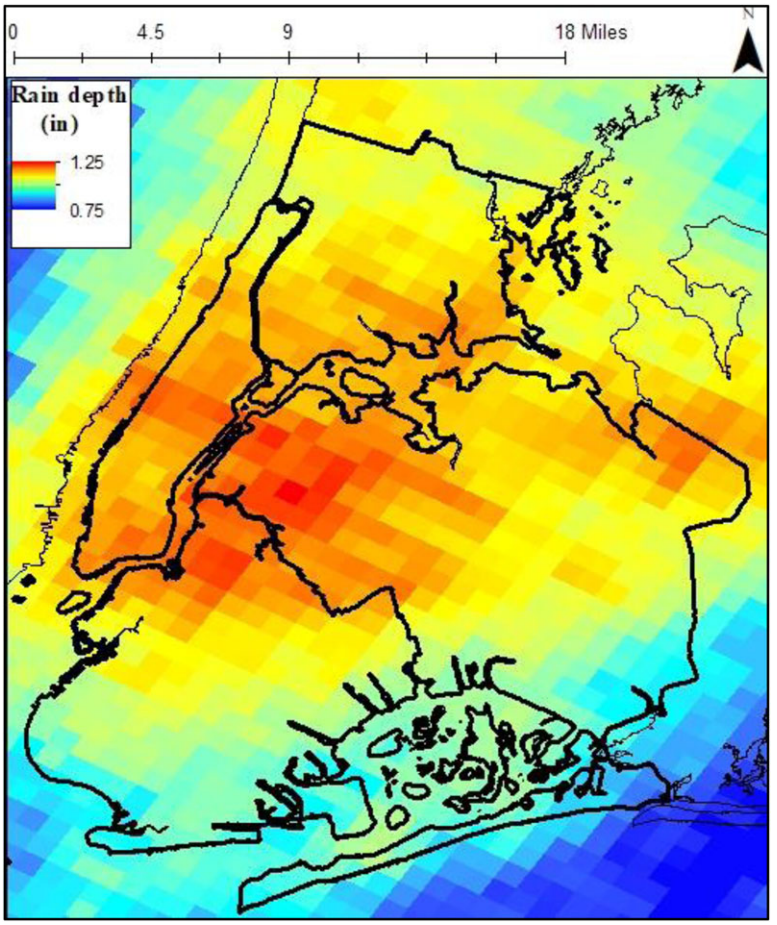

Figure 2.9. Daily average rainfall for days of known flooding (2001–2015). Rainfall data from Staten Island are missing due to a blocked radar band. Image adapted from Smith and Rodriguez (2017).

a high-resolution rainfall dataset for 1 km^2 and 15-min intervals was developed using warm season rainfall from 2001 to 2015 for the Fort Dix, NJ (KDIX) SR-88D (Weather Surveillance Radar, 1988 Doppler) radar in Mount Holly, New Jersey operated by the NWS (see Appendix 2.D for details of methods).

Baseline data for heavy downpours in New York City indicate a spatial variation in rainfall depth (Fig. 2.9). Days of known flooding (from Hazard Mitigation Reports and National Centers of Environmental Information (NCEI)) vary in rainfall depth between 0.9 and 1.25 inches across New York City. Rainfall on flooding days is at a maximum (1.25 inches) over the geographic center of the city (North Brooklyn and Northwest Queens), while some areas of high rainfall extend to the northeast. This region of high rainfall rates can be related to the urban impact on convective rainfall with higher rainfall within the city center. Figure 2.10 shows average maximum rainfall rates on days of known flooding at sub-daily timescales.

2.4.1.4 Heavy downpour projections. Predicting and understanding heavy downpours in New York City is difficult, and the science is not yet available to accurately project future heavy rainfall at 1- to 6-h timescales. Short-duration heavy downpours are likely more sensitive to atmospheric conditions than longer-duration extreme rainfall, and results from longer-duration studies are not directly applicable to shorter-duration rainfall (Westra *et al.*, 2014). Additionally, heavy downpours can vary spatially across the city, and therefore rainfall

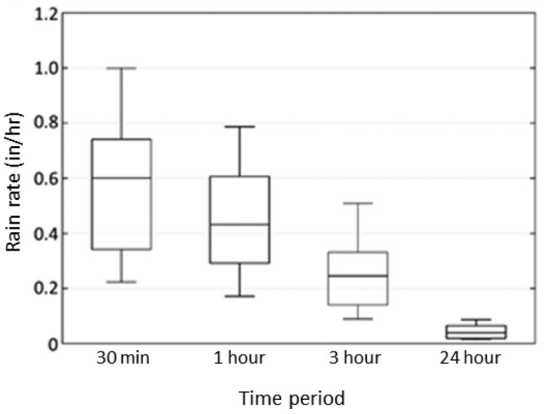

Figure 2.10. Boxplot for NYC-averaged max rainfall rates over 30 min, 1-, 3-, and 24-h for the 86 days of known flooding (2001–2015). Staten Island is excluded due to a blocked radar band. Whiskers represent the 10th and 90th percentiles, the box represents the 25th and 75th percentiles, and the line represents the median. Image from Smith and Rodriguez (2017).

results from Central Park may not be applicable across all five boroughs. Finally, when using rainfall projections for design purposes such as in the New York City Climate Resiliency Design Guidelines (NYC Mayor's Office of Recovery and Resiliency, 2018), it is important to recognize that smaller areas can experience higher rainfall rates than larger areas. This is often solved using Area Reduction Factors, which scale rainfall intensity by the areal extent of coverage (e.g. Wright *et al.*, 2013).

Urban impacts. Heavy downpours in New York City and other cities are affected by several physical processes including urban modification of rainfall and interactions with the land–sea boundary. Patterns of urban modification of rainfall have been found in Chicago (Changnon, 1968), Cleveland (Huff and Changnon, 1973), St. Louis (Changnon, 1979), San Antonio and Dallas (Shepherd *et al.*, 2002), Houston (Burian and Shepherd, 2005), Indianapolis (Niyogi *et al.*, 2011), Atlanta (Wright *et al.*, 2012; McLeod *et al.*, 2017), Baltimore (Smith *et al.*, 2012), and Charlotte (Wright *et al.*, 2013).

Urban areas can change rainfall patterns through UHI effects, urban-induced roughness (i.e., buildings interrupting air flow), and aerosols caused by pollution (Shepherd, 2005; Shepherd, 2013). These effects influence the path and development of thunderstorms, resulting in different rainfall patterns depending on the atmospheric setting. Generally, a weak UHI increases rainfall over city centers, while strong UHIs increase rainfall around the urban fringe, particularly downwind of urban areas (Bornstein and LeRoy, 1990; Shepherd, 2013). Short-duration heavy rainfall that produces flooding in urban areas is typically driven by warm-season thunderstorms with the most extreme rain rates occurring in the evening (Ntelekos *et al.*, 2007). These storms are also the most influenced by urbanization (Smith *et al.*, 2013).

A handful of studies have attempted to understand the spatial patterns of observed extreme rainfall in New York City as it is affected by urbanization. Bornstein and LeRoy (1990) investigated the impacts of the city on paths of thunderstorms. They found that the UHI can cause convection, or lifting of air, while the city roughness (buildings and structures) can induce divergence, or the separation of air; together these result in rainfall minima within the city and rainfall maxima surrounding and downwind of the city, especially on days with a strong UHI (Bornstein and LeRoy, 1990).

Yeung *et al.*, 2011, used high-resolution radar rainfall fields from the Fort Dix, NJ radar and Weather Research and Forecasting modeled storm events to investigate the role of urban areas on convective storm tracks in the greater New York City region. The results showed an increased number of days exceeding 1 inch of rainfall over New York City (on average, 9 days per summer season).

Recently, 1-h, 4 km^2 multisensor Stage IV rainfall data (Lin and Mitchell, 2005) were used to classify rainfall in New York City down to 1-h events (Hamidi *et al.*, 2017). The results showed that rainfall extremes have substantially higher rainfall rates at a 1-h scale in summer, and that summer extreme rainfall is more localized and associated with frontal systems than is winter extreme rainfall. Furthermore, Queens is most likely, and Staten Island is least likely, to experience high-intensity large areal extent 1-h summertime precipitation extremes (Hamidi *et al.*, 2017).

Land–sea boundary effects. The land–sea boundary also plays an important role in storm development and spatial patterns of extreme rainfall. The sea breeze can cause air to converge at low levels, thus creating uplift for thunderstorms (Weckwerth, 2000) and producing strong convection (Wilson and Megenhardt, 1997). In regions with both

urbanization and land–sea boundaries to the east, the land–sea boundary tends to increase convergence, provide a source of moisture for thunderstorms, and increase rainfall intensity (Ryu *et al.*, 2016). It is difficult, however, to disentangle the effects of sea breezes and the urban influence, as urbanization can affect the location of sea-breeze fronts (Carter *et al.*, 2012). Furthermore, New York City's location with its multiple water bodies creates an array of different sea breeze fronts across the city (Colle *et al.*, 2003; Novak and Colle, 2006). In the case of New York City, where the sea breeze generally is located to the southeast of the urban center, cooler air tends to stabilize the lower layers of incoming thunderstorms, generally causing them to weaken as they cross the city center (D. Rind, personal communication).

2.4.1.5 Effects of climate change on heavy downpours. Climate change is likely to influence the complex dynamics of urban and sea breeze–modified heavy downpours. Heavy downpours are closely tied to the amount of available moisture in the air, which is in turn influenced by air temperature. As the climate warms, the Clausius–Clapeyron relationship indicates that a warmer atmosphere can have higher ratios of water vapor to air at saturation; this is likely to increase rates of heavy downpours with climate change (Trenberth *et al.*, 2003).

However, increases of rainfall intensity with temperature have been observed at much higher ratios than predicted by the Clausius–Clapeyron equation, especially for sub-daily extreme rainfall (Westra *et al.*, 2014). It has also been projected that there will be more convective storms over the Northeast United States during the later 21st century (Li and Colle, 2016), which will additionally increase heavy downpours and flooding.

Interactions between these complex mechanisms are difficult to predict, but some paths forward have been proposed (Arnbjerg-Nielsen *et al.*, 2013). These include a determination of the storm types that drive extreme rainfall in New York City (Figs. 2.6 and 2.7). This will help to clarify a path forward and should be considered in future work of the NPCC.

2.4.2 Urban flooding

Increases in extreme rainfall are expected to increase urban flooding because an increase in water volume should increase flood peaks (Ashley *et al.*, 2005; Melillo *et al.*, 2014). At national and regional scales, however, the ability to detect this trend is difficult. Several studies have examined streamflow records for a connection between high-flow events and climate change at national and regional scales. While some studies have found significant trends in high-flow streamflow (Groisman *et al.*, 2001a; Groisman *et al.*, 2001b; Juckem *et al.*, 2008; Sagarika *et al.*, 2014), others have not (Douglas *et al.*, 2000; McCabe and Wolock, 2002; Small *et al.*, 2006; Villarini *et al.*, 2009; Hirsch and Ryberg, 2011).

These studies typically analyze watersheds that are undisturbed, but a few regional studies have attempted to discern changes in the urban flood record with climate change (Yang *et al.*, 2013 in Milwaukee; Rouge and Cai, 2014 in Chicago). Yang notes that for changes in flood response it is difficult to disentangle signals of "large-scale climate change, regional climate change induced by urbanization, and contrasting runoff generation mechanisms associated with land surface properties."

Urban flooding was not covered in NPCC2. Here, NPCC3 establishes current baselines and past trends in urban flooding for New York City and the surrounding area. These can be used in the next generation of projections for urban flooding that will be derived from quantitative projections of heavy downpours to be developed by NPCC4.

2.4.2.1 Urban flooding past trends and baselines. In order to investigate trends, streamflow data for flash flooding in small watersheds near New York City was used as a proxy (see Appendix 2.E). Annual peak streamflows in several small (less than 15 km^2) watersheds in the U.S. Census-designated New York City urban region were analyzed for change points and statistically significant trends, similarly to the heavy downpour rainfall data.

Trends in urban flooding are difficult to establish via this flash flooding proxy (for full results see Appendix 2.D). One New York City–region stream record, for the Mahwah River near Suffern, NY, has a statistically significant change point in 1967, which is similar to the change point in rainfall extremes (see Section 2.4.1.3). A different stream, Jumping Brook near Neptune City, NJ, has a statistically significant negative trend in annual peaks. Changes in annual peaks vary across the 14 streams with both increasing and decreasing change points and trends.

These changes are likely to be less representative of climate change (which would show more consistent patterns across the streams) and are more representative of a direct human impact on flash flooding. Nearly all the streams are highly managed through regulations, upstream diversions, and channel modifications. These urbanization effects, including the effects of impervious surfaces (Leopold, 1968), are likely to have larger impacts on the frequency and intensity of flash floods than does climate change (e.g., Yang *et al.*, 2013; Rouge and Cai, 2014).

Futhermore, the combination of urbanization and climate change requires flooding and stormwater management to be assessed in a nonstationary framework—that is a framework in which historic flood and runoff occurrence is not strictly relied upon to predict the probability of future flooding events (Milly *et al.*, 2008). This appears to be particularly evident with compound flooding (flooding caused by the combination of heavy downpours and storm surge) occurrence. Research has shown the number of compound flooding events in New York City to be increasing as weather patterns shift and sea levels rise, to cause larger precipitation amounts and more storm surge (Wahl *et al.*, 2015).

Urban flooding baselines and variation across the city were analyzed using 311 flood report data (https://data.cityofnewyork.us/Social-Services/311-Service-Requests-from-2010-to-Present/erm2-nwe9). Typically, urban flooding is detected as a quick rise in stream depth or flow over a certain threshold (as used in Appendix 2.D). However, within the limits of New York City, there are no small stream channels to use for flood analyses. A major source of flood data is the 311 database, which records citizen phone calls to report street or highway flooding.

These 311 flood calls are biased due to two major issues. First, population density differences across the city make floods much more likely to be seen and reported in dense areas of the city. Second, different communities may report flooding at different rates due to perceptions of the likelihood of a response to their reports. These differences in reporting can also be observed in other types of 311 calls; for example, noise complaints, broken street lights, and other reports are also geographically biased.

This underlying bias of all types of 311 reports was used to correct the bias in flooding 311 reports. The number of 311 flood calls within a 1 km^2 area around a point was divided by the number of all 311 calls within the same area (Fig. 2.11). This allows for a distinction of how often floods are reported as compared to other 311 issues.

Additionally, the New York City 2019 Hazard Mitigation Plan with its annual updates and flood reports from the National Climatic Data Center (https://www.ncdc.noaa.gov/stormevents/) were used to define days of known flooding. These reports are generated by experts (NWS staff and emergency managers), which can make them more accurate. However, standards in reporting have changed over time, and event reporting has increased in more recent years.

Baseline data based on 311 calls for urban flooding indicate substantial spatial variation across New York City from 2004 to 2015 (Fig. 2.11). Flooding appears to occur most often in areas near the coast and areas without combined sewers: Staten Island, Jamaica Bay, and eastern Queens. The flooding pattern has been analyzed in comparison to rainfall and other potential factors, including elevation, impervious surfaces, and population density, to determine the drivers of flooding in New York City (Smith and Rodriguez, 2017). Results indicate that high groundwater tables influence flooding along the coast, while intense 1-h to 1-day rainfalls cause flooding farther inland. Flooding in Staten Island is primarily caused by wintertime extratropical cyclones (Smith and Rodriguez, 2017).

Results from the 311 data indicate that differences in flooding across the city are likely related to rainfall patterns, proximity to the coast, impervious coverage, and differing sewer coverage. The New York City 2019 Hazard Mitigation Plan additionally includes irregular topography, soil infiltration rate, and soil storage capacity as factors that influence flooding location. Figure 2.11 indicates the similar patterns between flood occurrence and sewer type, including: combined sewers, which collect both sewage and stormwater into one system; separate sewers, which have separate systems for sewage and stormwater; parks, which do not require sewers; and other, which includes any other means of stormwater conveyance, including direct drainage into local waterways.

2.4.3. *Future research on heavy downpours and urban flooding*

Improved projections of future heavy downpours and urban flooding in New York City will require

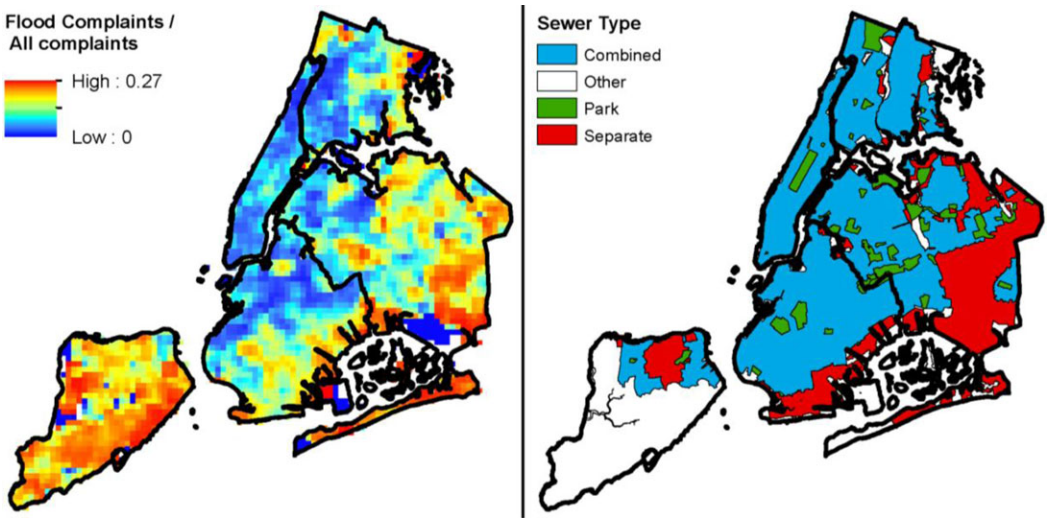

Figure 2.11. **Flood observations based on 311 calls for the period 2004–2015. Left panel: Flood observations based on 311 calls, normalized by all 311 observations. Units are in flood observations per all observations in 1 km^2; Right panel: New York City sewer type. Image from Smith and Rodriguez (2017).**

substantially more research. Potential areas of future research include:

Heavy downpours

- *Analysis of natural climate variability.* A more complete characterization is needed of present-day variability in storms and flooding. Because the New York metropolitan region experiences such large shifts in temperatures due to the annual cycle as well as large year-to-year variability per season, it is often difficult to determine the strength of the signal of climate change relative to the noise of natural climate variability. Quantifying this relationship for different precipitation metrics would help decision-makers prioritize hazard-specific responses to the projected changes.
- *Precipitation downscaling.* Results from GCMs can be dynamically downscaled, in which the outputs from the GCMs are used to force higher-resolution RCMs centered around the area of interest. The RCMs should include urban features related to the New York metropolitan region, such as its large proportion of impervious surface, tall buildings, and location near the sea. The proposed future methods for extreme heat events could be used as a basis for projecting heavy downpours as well. However, research in this area should evaluate how well RCMs can be used in conjunction with GCMs for projections of heavy downpours and urban flooding.
- Given that daily precipitation maxima are associated primarily with extra-tropical cyclones, research could assess whether there has been any convergence in global climate model projections on future storm track changes relevant to New York City.

Urban flooding

- *Urban flood modeling.* While projecting future heavy downpours is a task that requires substantially more research, modeling urban flooding in New York City may be developed in the near future. Several open-source academic models exist or are in development (e.g., Downer and Ogden, 2004; Goodrich *et al.*, 2010; Sanders *et al.*, 2008), and commercial urban flood models (MIKE SHE, InfoWorks ICM) are available as well. Utilization of such models will allow for understanding more clearly the relationships between rainfall intensity, duration, and frequency, and their effects on urban flooding in the region. These models could be used to assess current and future flood

risks as heavy downpour projections become available.[d]

- *Increased urban flood observations.* It is difficult to determine urban flood risk in New York City and to validate urban flood models due to lack of data. Urban flooding is typically measured by depth of streamflow in small catchment streams, but this is difficult in New York City because its surface streams have been buried. Recent advances in environmental sensing using microcontrollers may indicate a path forward for urban flood data collection. In recent years, there have also been substantial efforts to identify flood risk outside the typical streamflow methods through citizen science reporting (Cheung *et al.*, 2016; Poser and Dransch, 2010).

2.5 Droughts

NPCC1 reported the potential future changes in droughts for the city using the 12-month average Palmer Drought Severity Index (PDSI) (NPCC, 2010). It was projected that the frequency of drought will approximately double by the 2050s and will be five times greater by the 2080s. This NPCC3 report focuses on drought indices developed for the city's major reservoir system using paleoclimate data.

The drought of record in the New York metropolitan region is the one that occurred in the early to mid-1960s (Namias, 1966). It stands as a warning of the potential vulnerability of New York City to severe water shortages. Many of the operating rules governing water management for the region depend largely on performance testing using the 1960s drought as the standard (Kolesar and Serio, 2011, Devineni *et al.*, 2013, Ravindranath *et al.*, 2016).

Since reliable observed streamflow data in the region often date back only to the 1950s, this section addresses questions as to the longer-term drought risk including the characterization of drought duration, severity and return period through paleoclimate data analyses.

Hydrologic reconstructions of streamflow from tree-rings spanning the past several centuries can provide a more complete picture of the range of variability at the decadal or longer time scales. Other paleoclimate studies using pollen assemblages suggest drought conditions from ~800 to 1300 AD as well (Pederson *et al.*, 2005).

These paleoclimate studies can place the short instrumental record into a more long-term perspective. Previous work (Devineni *et al.*, 2013, Woodhouse *et al.*, 2006, Nowak *et al.*, 2012; Stockton and Jacoby, 1976) have demonstrated the utility of paleo climate streamflow reconstructions in providing a more objective evaluation of operating rules for reservoir systems. Consequently, for NPCC3, we developed reconstructions of the Pepacton, Cannonsville, and Neversink (PCN) reservoir inflows (Fig. 2.12) using tree-ring chronologies in the upper Delaware River basin.[e] We used these extended reservoir inflow records to develop long-term drought profiles on duration, severity and return periods under different water demand thresholds. Table 2.8 provides key definitions for terms used to discuss drought throughout this section.

2.5.1 Methods of analysis

This section briefly presents the methodology employed for reconstructing reservoir inflow and for deriving drought indicators. Data description and technical details of the model structure are provided in Appendix 2.E. Full details of the methods can be found in Devineni *et al.* (2013).

2.5.1.1 Reservoir inflow reconstructions. We developed the PCN reservoir inflow reconstructions using a statistical regression model. Instrumental data (i.e., inflows for the three reservoirs during the observation period since 1928) were provided by the New York City Department of Environmental Protection. Tree-ring width measurements that represent paleoclimate data for the Delaware watershed date back to 1754. These are available from the Tree Ring Laboratory at the Lamont-Doherty Earth Observatory (LDEO).

[d]See the following website for information about the Town & Gown: Citywide Stormwater Resiliency study: https://www1.nyc.gov/assets/ddc/downloads/town-and-gown/active-rfps/CitywideStormwaterResiliencyStudyT+GRFP.pdf

[e]While this NPCC report uses the Delaware River Basin as a drought proxy for the New York metropolitan region, the city measures and monitors water supply availability on a whole-system basis including the Delaware, Catskill and the Croton systems.

Table 2.8. NPCC3 drought definitions

Term	Definition
Reservoir inflow	Streamflow (amount of water) coming into reservoirs.
Reconstruction	Estimate of streamflow for past period using trees proven to be good estimators of observed streamflow during the period of gauged record. This is typically developed using statistical models that capture the relationship between tree growth index and the observed streamflow record during the overlapping period. This statistical model is applied to the prior period.
Cumulative deficit	Accumulated water deficit over an *n*-year period. Deficit for each year is defined as the difference between water demand (reservoir releases) and water supply (reservoir inflows).

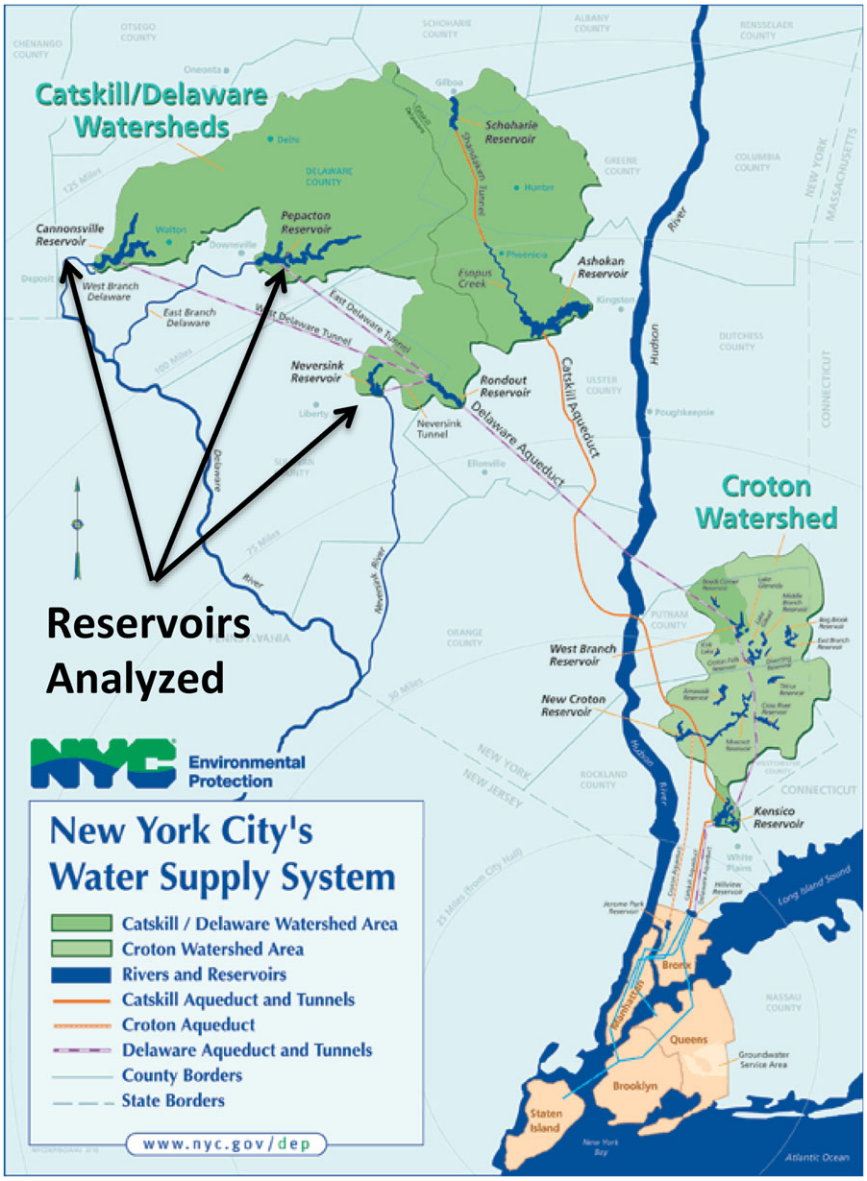

Figure 2.12. New York City's Water supply system. The Cannonsville, Pepacton, and Neversink reservoirs of the Delaware Watershed are analyzed by NPCC3 using long-term drought records from tree-ring data. *Source: NYCDEP.*

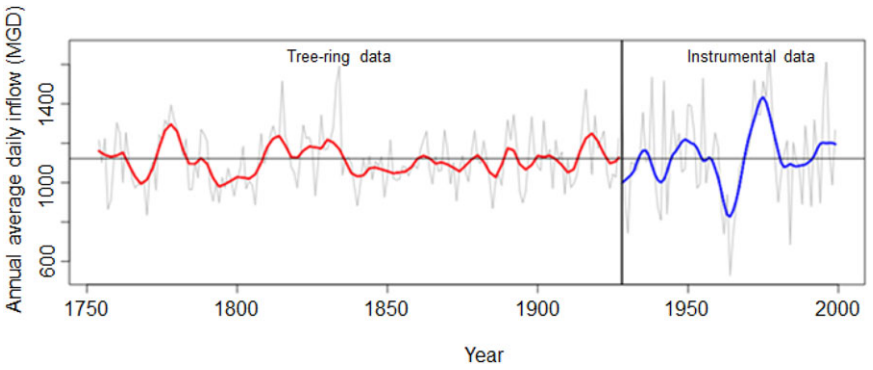

Figure 2.13. Reconstruction of combined annual average daily inflow from eight tree-ring chronologies in the Pepacton, Cannonsville, and Neversink reservoirs, which supply approximately 50% of the New York City water supply (DRBC 2018). Since tree growth is dependent on climate and since each tree-ring represents a season of growth, tree-ring measurements provide information on hydrological indicators over a tree's life span that can be used to understand variations in climate.

Given data from the three reservoirs and eight local tree-ring chronologies as predictor variables, the statistical model provides regression equations for each reservoir that are used to reconstruct the streamflow. The period over which the reconstruction was done is 1754–1927. The resulting outputs are simulations of annual average daily streamflow from 1754 to 2000 for the three reservoirs.

2.5.1.2 Drought indicators. We constructed a drought index to characterize the regional drought with explicit consideration of water demand. We developed the drought index on instrumental streamflow data first to gain an understanding of the observed drought risk since 1928. Then, we applied it to the reservoir inflows reconstructed from the tree-ring data.

2.5.2 Results

This section presents the results of the streamflow reconstructions and drought analyses for the instrumental period and the paleo-reconstructed period.

2.5.2.1 Combined inflows from tree-ring data and incidence of observed drought. The general trends of combined reservoir inflow from tree-ring data from 1754 to 2000 are shown in Figure 2.13. While the 1960s drought is the most severe in the extended record, the tree-ring analysis show that there were regimes with less severe but longer drought durations (e.g., 1830–1860, 1790–1810).

By examining this historical record, we found that there are at least eight incidences of historical drought lasting 5 consecutive years or longer occurring in the region since 1750 (Table 2.9). Six of these occurred in the paleo record period, and two were observed in the instrumental period. This indicates there is a potential for persistent drought in the New York metropolitan region in the future.

Table 2.9. Incidence of historical drought of at least 5 consecutive years in the New York metropolitan region in the paleo record (1754–1927) and the instrumental record (1928–1999)

Drought duration	Years
Paleo record	
10 years	1764–1773
11 years	1791–1801
5 years	1803–1807
9 years	1852–1860
6 years	1883–1888
5 years	1909–1913
Instrumental record	
5 years	1929–1933
7 years	1961–1967

2.5.3 Summary and future work

Long-term drought risk for the New York City water supply system is developed based on tree-ring reconstructions for PCN reservoir inflows. The streamflow reconstructions reveal droughts with a longer duration than the 7-year major drought seen in the instrumental period (1961–1967). If the variability of streamflow as seen from the long paleoclimate tree-ring record (246 years) were to continue into the future, increases in regional water demand due to population increase and climate change could

affect the duration of droughts. This is important from a drought risk and planning perspective.

Hydrologic reconstructions provide a more complete picture of how streamflows have varied in the New York metropolitan region water supply area. However, longer-term water planning decisions should also be informed by climate scenarios, such as the New York City Panel on Climate Change (Moody and Brown, 2012; Steinschneider and Brown, 2012; NAS, 2018; Rosenzweig and Solecki, 2018).

Given current understanding of seasonal to interannual climate variability, and of climate change, NPCC4 could develop an approach for regularly updating the drought estimates using climate observations and models tuned to prediction at different timescales. Consequently, future work should involve drought risk characterization and modeling that embraces paleo-reconstructions, climate model hindcasts utilizing such metrics as PDSI, observed trends, and near-term and longer-term projections in a rigorous way to understand climate risk and formulate management and adaptation strategies at decision-relevant scales.

2.6 Conclusions and recommendations

NPCC3 confirms the use of NPCC2 projections as those of record for decision-making in the City of New York. It analyzed how recent climate trends compare to the projections for the region. Further, it has begun to develop and test new methods for observations and projections to be used in resilience planning. Using expanded observations, bias correction, and RCMs, these methods can provide quantitative analyses for heat extremes, heavy downpours, and droughts. They are available for developing the next full set of NPCC projections.

Based on these and other methods, the next generation of global and RCM outputs will be used in upcoming NPCC assessments to create a new unified set of projections for decision making in the New York metropolitan region. The methods tested by NPCC3 utilizing GCM and RCM ensembles and scenarios will enable the updated identification of climate change "hotspots" of vulnerability at finer spatial scales within the city and across the region.

However, GCMs may not yet be able to simulate the forcings required for RCMs to model some finer-scale extreme events such as convective thunderstorms.

Key findings

Observations and projections

- Observed annual temperature and precipitation trends between 2010 and 2017 fell largely within the NPCC2 projected range for the 2020s time period. [These comparisons should be viewed with caution because of the role that natural variation plays in the short term.]
- Observations of increasing heavy rainfall between 2011 and 2017 fell largely within the NPCC2 projected range 2020s time period. [These comparisons should be viewed with caution because of the role that natural variation plays in the short term.]
- NPCC3 confirms the use of the NPCC2 2015 projections for decision-making by the city and region.

Extreme heat

- Increasing decadal trends in annual daily average maximum summer temperatures in June, July, and August varied across the city. Central Park has experienced an increasing trend of 0.2 °F per decade from 1900 to 2013. Since 1970, JFK average annual daily maximum summer temperatures have been rising at a rate of 0.5 °F per decade, and LaGuardia at 0.7 °F per decade.
- New projection methods for extreme heat events were developed and tested for the New York metropolitan region. The test includes bias correction, a method that adjusts the mean and variance of GCM results to match a representative set of observations from the region, and high-resolution regional climate modeling.

Heavy downpours

- New studies support NPCC2 projected increases in precipitation, in terms of the mean and extremes for the region. These precipitation changes are expected to occur in both the winter and summer seasons. However, uncertainty in these precipitation projections is larger than the uncertainty in temperature projections.
- A change point in sub-daily heavy rainfall events can be detected at the Central Park rain gauge in the mid-1960s for the annual maxima of 3-hourly rainfall; the only significant trend

found was for 3-h annual maximum rainfall depth at the JFK rain gauge.
- Extratropical cyclones cause the largest number of extreme 24-h precipitation events in New York City in every month out of the year.
- Rainfall that drives urban and flash flooding in the Northeast is typically temporally and spatially concentrated and is most often caused by thunderstorms.
- Days of known flooding vary spatially across New York City in rainfall depth between 0.9 and 1.25 inches. Rainfall on flooding days is at a maximum (1.25 inches) over the geographic center of the city (North Brooklyn and Northwest Queens).
- Urban flooding appears to occur most often in areas near the coast and areas without combined sewers: Staten Island, Jamaica Bay, and eastern Queens. Results from 311 call data indicate that differences in flooding across the city are likely related to rainfall patterns, proximity to the coast, impervious surfaces, and differing sewer coverage.
- The groundwork for future projections was established by refocusing the discussion from daily to sub-daily rainfall extremes.

Droughts

- While there has not been a major drought since the 1960s in the New York metropolitan region, analysis based on tree-rings from about the last 250 years shows that 10-year or longer droughts have occurred. Thus, the possibility of future droughts should be considered in planning.

Recommendations for research

- Future NPCC research can improve the utility of quantitative heat wave projections by working with the New York City Department of Health and Mental Hygiene and the National Weather Service (NWS). Together these groups can investigate how best to evaluate need for future revisions of heat advisory criteria that consider changing combined effects of temperature and humidity (i.e., heat index).
- Relevant research areas include examination of thresholds of heat and humidity effects on human health, and strategies to design interventions that will be effective in New York City's hotter climate.
- Research is needed to determine benchmarks for sub-hourly extreme precipitation and associated flooding events using satellite data and rain gauges at Central Park, LaGuardia, JFK, and Newark. Using these benchmarks, researchers should aim to improve sub-hourly extreme precipitation projections that consider urban meteorological effects and identify neighborhoods likely to be flooded.
- Improved characterization is needed of likely large-scale conditions that may lead to extreme drought based on further tree-ring analysis in the region.

References

Anderson, G.B. & M.L. Bell. 2010. Heat waves in the United States: mortality risk during heat waves and effect modification by heat wave characteristics in 43 U.S. Communities. *Environ. Health Perspect.* **119:** 210–218.

Arnbjerg-Nielsen, K., P. Willems, J. Olsson, *et al.* 2013. Impacts of climate change on rainfall extremes and urban drainage systems: a review. *Water Sci. Technol.* **68:** 16–28.

Arnfield, A.J. & C.S.B. Grimmond. 1998. An urban canyon energy budget model and its application to urban storage heat flux modeling. *Energy Build.* **27:** 61–68.

Ashley, R.M., D.J. Balmforth, A.J. Saul & J.D. Blanskby 2005. Flooding in the future–predicting climate change, risks and responses in urban areas. *Water Sci. Technol.* **52:** 265–273.

Bauer, M., G. Tselioudis & W.B. Rossow. 2016. A new climatology for investigating storm influences in and on the extratropics. *J. Appl. Meteorol. Clim.* **55:** 1287–1303.

Bornstein, R.D. & G. LeRoy. 1990. Urban barrier effects on convective and frontal thunderstorms. Preprints. In *Fourth Conference on Mesoscale Processes*, American Meteor Society, Boulder, CO, 120–121.

Boyle, J. 1986. Comparison of the synoptic conditions in mid-latitudes accompanying cold surges over eastern Asia for the months of December 1974 and 1978. Part I: monthly mean fields and individual events. *Mon. Weather Rev.* **114:** 903–930.

Bruyère, C.L., J.M. Done, G.J. Holland & S. Fredrick. 2014. Bias corrections of global models for regional climate simulations of high-impact weather. *Clim. Dyn.* **43:** 1847–1856.

Bruyère, L., J. Monaghan, F. Steinhoff & D. Yates. 2015. Bias-corrected CMIP5 CESM data in WRF/MPAS intermediate file format.

Burian, S. & J. Shepard. 2005. Effect of urbanization on the diurnal rainfall pattern in Houston. *Hydrol. Process.* **19:**1089–1103.

Carter, M., J.M. Shepherd, S. Burian & I. Jeyachandran. 2012. Integration of lidar data into a coupled mesoscale land surface model: a theoretical assessment of sensitivity of urban–coastal mesoscale circulations to urban canopy parameters. *J. Atmos. Oceanic Technol.* **29:** 328–346.

Castellano, C.M. & A.T. DeGaetano. 2017. Downscaling extreme precipitation from CMIP5 simulations using historical analogs. *J. Appl. Meteorol. Clim.* https://doi.org/10.1175/JAMC-D-16-0250.

Castellano, C. & A. DeGaetano. 2015. *Downscaled Projections of Extreme Rainfall in New York State*. Ithaca, NY: Northeast Regional Climate Center.

Changnon, S.A. 1968. The LaPorte weather anomaly—fact or fiction? *Bull. Am. Meteorol. Soc.* **53:** 246–251.

Changnon, S. 1979. Rainfall changes in summer caused by St. Louis. *Science* **205:** 402–404.

Chen, S., W. Chen & K. Wei. 2013. Recent trends in winter temperature extremes in eastern China and their relationship with the Arctic Oscillation and ENSO. *Adv. Atmos. Sci.* **30:** 1712–1724.

Cheung, W., D. Houston, J.E. Schubert, *et al.* 2016. Integrating resident digital sketch maps with expert knowledge to assess spatial knowledge of flood risk: a case study of participatory mapping in Newport Beach, California. *Appl. Geogr.* **74:** 56–64.

Childs, P.P. & S. Raman. 2005. Observations and numerical simulations of urban heat island and sea breeze circulations over New York City. *Pure Appl. Geophys.* **162:** 1955–1980.

Colle, B.A., J.B. Olson & J.S. Tongue. 2003. Multiseason verification of the MM5. Part I: comparison with the Eta model over the central and eastern United States and impact of MM5 resolution. *Weather Forecast.* **18:** 431–457.

Davis, R.E., G.R. McGregor & K.B. Enfield. 2016. Humidity: a review and primer on atmospheric moisture and human health. *Environ. Res.* **144:** 106–116.

Dee, D.P. & co-authors. 2011. The ERA interim reanalysis: configuration and performance of the data assimilation systems. *Quart. J. Roy. Meteor. Soc.* **137:** 553–597.

Downer, C.W. & F.L. Ogden. 2004. GSSHA: model to simulate diverse stream flow producing processes. *J. Hydrol. Eng.* **9:** 161–174.

DeGaetano, A.T. & C.M. Castellano. 2017. Future projections of extreme precipitation intensity-duration-frequency curves for climate adaptation planning in New York State. *Clim. Serv.* **5:** 23–35.

Dickinson, R.E., A.H. Sellers, P.J. Kennedy & M.F. Wilson. 1986. Biosphere-atmosphere transfer scheme (BATS) for the NCAR Climate Community Model. NCAR Tech. Note NCAR/TN-2751STR, 69 pp.

de Vries, H., R.J. Haarsma & W. Hazeleger. 2012. Western European cold spells in current and future climate. *Geophys. Res. Lett.* **39**. https://doi.org/10.1029/2011GL050665.

Devineni, N., U. Lall, N. Pederson & E. Cook. 2013. A tree ring–based reconstruction of Delaware River basin streamflow using hierarchical Bayesian regression. *J. Clim.* **26:** 4357–4374.

Douglas, E.M., R.M. Vogel & C.N. Kroll. 2000. Trends in floods and low flows in the United States: impact of spatial correlation. *J. Hydrol.* **240:** 90–105.

DRBC. Basin information. Accessed June 15, 2018. https://www.state.nj.us/drbc/basin/.

Efthymiadis, D., C.M. Goodess & P.D. Jones. 2011. Trends in Mediterranean gridded temperature extremes and large-scale circulation influences. *Nat. Hazard. Earth Syst.* **11:** 2199–2214.

Etienne, E., N. Devineni, R. Khanbilvardi & U. Lall. 2016. Development of a demand sensitive drought index and its application for agriculture over the conterminous United States. *J. Hydrol.* **534:** 219–229.

Fan, F., R.S. Bradley & M.A. Rawlins. 2014. Climate change in the northeastern US: regional climate model validation and climate change projections. *Clim. Dyn.* **43:** 145–161.

Fischer, E.M., S.I. Seneviratne, P.L. Vidale, *et al.* 2007. Soil moisture–atmosphere interactions during the 2003 European summer heat wave. *J. Clim.* **20:** 5081–5099.

Gao, Y., J.S. Fu, J.B. Drake, *et al.* 2012. Projected changes of extreme weather events in the eastern United States based on a high resolution climate modeling system. *Environ. Res. Lett.* **7**. https://doi.org/10.1088/1748-9326/7/4/044025.

Gedzelman, S.D., S. Austin, R. Cermak, *et al.* 2003. Mesoscale aspects of the urban heat island around New York City. *Theor. Appl. Climatol.* **75:** 29–42.

Giorgi, F., M.R. Marinucci, G.T. Bates & G.D. Canio. 1993. Development of a second-generation regional climate model (RegCM2). Part II: convective processes and assimilation of lateral boundary conditions. *Mon. Wea. Rev.* **121:** 2814–2832.

Goodrich, D.C., C.L. Unkrich, R.E. Smith, D.P. Guertin, M. Hernandez, I.S. Burns, J.E. Massart, L. Levick, S.N. Miller, D.J. Semmens & W.G. Kepner. 2010. The AGWA-KINEROS2 suite of modeling tools. In *Watershed Management 2010: Innovations in Watershed Management under Land Use and Climate Change*, 1294–1305.

Groisman, P.Y., R.W. Knight & T.R. Karl. 2001a. Heavy precipitation and high streamflow in the contiguous United States: Trends in the 20th century. *Bull. Am. Meteorol. Soc.* **82:** 219–246.

Groisman, P.Y., R.W. Knight, T.R. Karl, *et al.* 2001b. Contemporary changes of the hydrological cycle over the contiguous United States: trends derived from *in situ* observations. *J. Hydrometeorol.* **5:** 64–85.

Gutiérrez, E., A. Martilli, J.L. Santiago & J.E. González. 2015a. A mechanical drag coefficient formulation and urban canopy parameter assimilation technique for complex urban environments. *Bound. Layer Meteorol.* **157:** 333–341.

Gutiérrez, E., J.E. González, A. Martilli & R. Bornstein. 2015b. On the anthropogenic heat fluxes using an air conditioning evaporative cooling parameterization for mesoscale urban canopy models. *J. Sol. Energy Eng.* **137:** http://doi:10.1115/1.4030854.

Hall, T. & J.F. Booth. 2017. SynthETC: a statistical model for severe winter storm hazard on Eastern North America. *J. Clim.* **30:** 5329–5343.

Hamidi, A., N. Devineni, J. Booth, *et al.* 2017. Classifying urban rainfall extremes using weather radar data: an application to the Greater New York Area. *J. Hydrometeor.* **18:** 611–623.

Hass, A., K. Ellis, L. Reyes Mason, *et al.* 2016. Heat and humidity in the city: neighborhood heat index variability in a mid-sized city in the Southeastern United States. *Int. J. Environ. Res. Public Health* **13:** 117.

Hawkins, E., T.M. Osborne, C.K. Ho & A.J. Challinor. 2013. Calibration and bias correction of climate projections for crop modelling: an idealised case study over Europe. *Agric. Forest Meteorol.* **170:** 19–31.

Hirsch, R.M. & K.R. Ryberg. 2011. Has the magnitude of floods across the USA changed with global CO2 levels? *Hydrol. Sci. J.* **57:** 1–9.

Holland, G., J. Done, C. Bruyère, *et al.* 2010. Model investigations of the effects of climate variability and change on future Gulf of Mexico tropical cyclone activity. Offshore Technology Conference. Accessed May 12, 2017. http://www.onepetro.org/doi/10.4043/20690-MS.

Hong, S.-Y. & J.-O.J. Lim. 2006. The WRF Single-moment 6-class Microphysics Scheme (WSM6). *Asia Pac. J. Atmos. Sci.* **42:** 129–151.

Haurwitz, B. 1947. Comments on the sea breeze circulation. *J. Meteorol.* **4:** 1–8.

Horton, R., D. Bader, Y. Kushnir, C. Little, R. Blake & C. Rosenzweig. 2015. New York city panel on climate change 2015 report. Chapter 1: climate observations and projections. *Ann. N.Y. Acad. Sci.* **1336:** 18–35.

Huff, F. & S. Changnon. 1973. Precipitation modification by major urban areas. *Bull. Am. Meteorol. Soc.* **54:** 1220–1232.

Ichinose, T., K. Shimodozono & K. Hanaki. 1999. Impact of anthropogenic heat on urban climate in Tokyo. *Atmos. Environ.* **33:** 3897–3909.

IPCC. 2013. *Climate Change 2013: The Physical Science Basis. Contribution of Working Group I to the Fifth Assessment Report of the Intergovernmental Panel on Climate Change* [Stocker, T.F., D. Qin, G.-K. Plattner, M. Tignor, S.K. Allen, J. Boschung, A. Nauels, Y. Xia, V. Bex and P.M. Midgley (eds.)]. Cambridge University Press, Cambridge, United Kingdom and New York, NY, USA, 1535 pp. https://doi.org/10.1017/CBO9781107415324.

Juckem, P.F., R.J. Hunt, M.P. Anderson & D.M. Robertson. 2008. Effects of climate and land management change on streamflow in the driftless area of Wisconsin. *J. Hydrol.* **355:** 123–130.

Kain, J.S. 2004. The Kain–Fritsch convective parameterization: an update. *J. Appl. Meteorol.* **43:** 170–181.

Kendall, M.G. 1975. *Rank Correlation Methods.* London: Charles Griffin.

Kimura, F. & A. Kitoh. 2007. Downscaling by pseudo global warming method. The Final Report of the ICCAP. *Final Rep.* 43–46.

Knowlton, K., B. Lynn, R.A. Goldberg, *et al.* 2007. Projecting heat-related mortality impacts under a changing climate in the New York City region. *Am. J. Public Health* **97:** 2028–2034.

Kolesar, P. & J. Serio. 2011. Breaking the deadlock: Improving water-release policies on the delaware river through operations research. *Interfaces* **41:** 18–34.

Konrad, C.E. 1996. Relationships between the intensity of cold-air outbreaks and the evolution of synoptic and planetary-scale features over North America. *Mon. Weather Rev.* **124:** 1067–1083.

Kretschmer, M., D. Coumou, L. Agel, *et al.* 2018. More-persistent weak stratospheric polar vortex states linked to cold extremes. *AMS BAMS.* **99:** 49–60. https://doi.org/10.1175/bams-d-16-0259.1.

Kunkel, K.E., D.R. Easterling, D.A.R. Kristovich, B. Gleason, L. Stoecker & R. Smith. 2012. Meteorological causes of the secular variations in observed extreme precipitation events for the conterminous United States. *J. Hydrometeor.* **13:** 1131–1141. https://doi.org/10.1175/JHM-D-11-0108.1.

Lombardo, K.A. & B.A. Colle. 2012. Ambient conditions associated with the maintenance and decay of quasi-linear convective systems crossing the northeastern U.S. coast. *Mon. Wea. Rev.* **140:** 3805–3819.

Leopold, L.B. 1968. *Hydrology for Urban Land Planning–A Guidebook on the Hydrologic Effects of Urban Land Use.* US Geological Survey.

Li, H. & B.A. Colle. 2016. Future changes in convective storm days over the Northeastern United States using linear discriminant analysis applied to CMIP5 predictions. *J. Clim.* **29:** 4327–4345.

Li, D. & E. Bou-Zeid. 2013. Synergistic interactions between urban heat islands and heat waves: the impact in cities is larger than the sum of its parts. *J. Appl. Meteorol. Climatol.* **52:** 2051–2064.

Lin, Y. & K.E. Mitchell. 2005. The NCEP stage II/IV hourly precipitation analyses: development and applications. In *19th Conference Hydrology*, American Meteorological Society, San Diego, CA.

Loucks, D.P., J.R. Stedinger & D.A. Haith. 1981. *Water Resource Systems Analysis.* Englewood Cliffs, NJ: Prentice-Hall.

Lorenz, R., E.B. Jaeger & S.I. Seneviratne. 2010. Persistence of heat waves and its link to soil moisture memory. *Geophys. Res. Lett.* **37**. https://doi.org/10.1029/2010GL042764.

Luber, G. & M. McGeehin. 2008. Climate change and extreme heat events. *Am. J. Prev. Med.* **35:** 429–435.

Lyons, B.A., A. Hasell & N.J. Stroud. 2018. Enduring extremes? Polar vortex, drought, and climate change beliefs. *Environ. Commun.* **12:** 876–894.

Mann, H.B. 1945. Non-parametric tests against trend. *Econometrica* **13:** 245–259.

Martilli, A., A. Clappier & M.W. Rotach. 2002. An urban surface exchange parameterisation for mesoscale models. *Bound. Layer Meteorol.* **104:** 261–304.

McCabe, G.J. & D.M. Wolock. 2002. A step increase in streamflow in the conterminous United States. *Geophys. Res. Lett.* **29:** 2185. https://doi.org/10.1029/2002GL015999.

McLeod, J., M. Shepherd & C.E. Konrad. 2017. Spatio-temporal rainfall patterns around Atlanta, Georgia and possible relationships to urban land cover. *Urban Clim.* https://doi.org/10.1016/j.uclim.2017.03.004.

Mearns, L.O., W.J. Gutowski, R. Jones, *et al.* 2009. A regional climate change assessment program for North America. *EOS.* **90:** 311–312.

Meehl, G.A. & C. Tebaldi. 2004. More intense, more frequent, and longer lasting heat waves in the 21st century. *Science* **305:** 994–997.

Melillo, J.M., T.C. Richmond & G.W. Yohe, Eds. 2014. *Climate Change Impacts in the United States: The Third National Climate Assessment. U.S.* Global Change Research Program, 841.

Milly, P.C., J. Betancourt, M. Falkenmark, *et al.* 2008. Stationarity is dead: whither water management? *Science* **319:** 573–574.

Moody, P. & C. Brown. 2012. Modeling stakeholder-defined climate risk on the Upper Great Lakes. *Water Resour. Res.* **48**. https://doi.org/10.1029/2012WR012497.

Morini, E., A. Touchaei, B. Castellani, *et al.* 2016. The impact of albedo increase to mitigate the urban heat island in Terni (Italy) using the WRF model. *Sustainability* **8:** 999. https://doi.org/10.3390/su8100999.

Moss, R.H. *et al.* 2010. The next generation of scenarios for climate change research and assessment. *Nature* **463:** 747–756.

Nakanishi, M. & H. Niino. 2006. An improved Mellor–Yamada level-3 model: its numerical stability and application to a regional prediction of advection fog. *Bound. Layer Meteorol.* **119:** 397–407.

Namias, J. 1966. Nature and possible causes of the northeastern United States drought during 1962–65. *Mon. Weather Rev.* **94:** 543–554.

NAS. 2018. Review of the New York City Department of Environmental Protection Operations Support Tool for Water Supply. Washington, DC: National Academies of Sciences, Engineering, and Medicine. The National Academies Press. https://doi.org/10.17226/25218.

New York City Panel on Climate Change (NPCC). 2010. Climate change adaptation in New York City. New York City panel on climate change 2010 report. *Annals of the New York Academy of Sciences.* 1196. New York, NY.

NYC Mayor's Office of Recovery & Resiliency. 2018. Climate resiliency design guidelines. Version 2.0. New York, NY: NYC ORR. https://www1.nyc.gov/assets/orr/pdf/NYC_Climate_Resiliency_Design_Guidelines_v2-0.pdf.

Ning, L., E.E. Riddle & R.S. Bradley. 2015. Projected changes in climate extremes over the northeastern United States. *J. Clim.* **28:** 3289–3310.

Ning, L. & R.S. Bradley. 2014. Winter precipitation variability and corresponding teleconnections over the Northeastern United States. *J. Geophys. Res. Atmos.* **119:** 7931–7945.

Niyogi, D., P. Pyle, M. Lei, *et al.* 2011. Urban modification of thunderstorms: an observational storm climatology and model case study for the Indianapolis urban region. *J. Appl. Meteorol. Clim.* **50:** 1129–1144.

Novak, D.R. & B.A. Colle. 2006. Observations of multiple sea breeze boundaries during an unseasonably warm day in metropolitan New York City. *Bull. Am. Meteorol. Soc.* **87:** 169–174.

Nowak, K., M. Hoerling, B. Rajagopalan & E. Zagona. 2012. Colorado River basin hydroclimatic variability. *J. Clim.* **25:** 4389–4403.

Ntelekos, A.A., J.A. Smith & W.F. Krajewski. 2007. Climatological analyses of thunderstoms and flash floods in the Baltimore metropolitan region. *J. Hydrometeorol.* **8:** 88–101.

Offerle, B., C.S.B. Grimmond & K. Fortuniak. 2005. Heat storage and anthropogenic heat flux in relation to the energy balance of a central European city centre. *Int. J. Climatol.* **25:** 1405–1419.

Oke, T.R. 1982. The energetic basis of the urban heat island. *Q. J. R. Meteorol. Soc.* **108:** 1–24.

Oke, T.R., B.D. Kalanda & D.G. Steyn. 1981. Parameterization of heat storage in urban areas. *Urban Ecol.* **5:** 45–54.

Ortiz, L.E., J.E. Gonzalez, W. Wu, *et al.* 2018. New York City impacts on a regional heat wave. *J. Appl. Meteorol. Climatol.* **57:** 837–851.

Overland, J., J.A. Francis, R. Hall, *et al.* 2015. The melting arctic and midlatitude weather patterns: are they connected? *J. Clim.* **28:** 7917–7932.

Pederson, D., D. Peteet, D. Kurdyla & T. Guilderson. 2005. Medieval warming, little ice age, and European impact on the environment during the last millennium in the lower Hudson Valley, New York, USA. *Q. Res.* **63:** 238–249.

Peterson, T.C., X. Zhang, M. Brunet India & J.L. Vázquez Aguirre. 2008. Changes in North American extremes derived from daily weather data. *J. Geophys. Res. Atmos.* 113. https://doi.org/10.1029/2007JD009453.

Pettitt, A.N. 1979. A non-parametric approach to the change-point problem. *Appl. Stat.* **28:** 126–135.

Poser, K. & D. Dransch. 2010. Volunteered geographic information for disaster management with application to rapid flood damage estimation. *Geomatica* **64:** 89–98.

Piani, C., G.P. Weedon, M. Best, *et al.* 2010. Statistical bias correction of global simulated daily precipitation and temperature for the application of hydrological models. *J. Hydrol.* **395:** 199–215.

Rouge, C. & X. Cai. 2014. Crossing-scale hydrological impacts of urbanization and climate variability in the Greater Chicago area. *J. Hydrol.* **517:** 13–27.

Ramamurthy, P., T. Sun, K. Rule & E. Bou-Zeid. 2015. The joint influence of albedo and insulation on roof performance: an observational study. *Energy Build.* **93:** 249–258.

Ramamurthy, P. & E. Bou-Zeid. 2016. Heatwaves and urban heat islands: a comparative analysis of multiple cities using a high-resolution numerical model. *J. Geophys. Res. Atmos.* **122:** 168–178.

Ramamurthy, P., J. González, L. Ortiz, *et al.* 2017. Impact of heatwave on a megacity: an observational analysis of New York City during July 2016. *Environ. Res. Lett.* **12**. https://doi.org/10.1088/1748-9326/aa6e59.

Ravindranath, A., N. Devineni & P. Kolesar. 2016. An environmental perspective on the water management policies of the upper Delaware River basin. *Water Policy* **18:** 1399–1419.

Riahi, K. *et al.* 2011. RCP 8.5—a scenario of comparatively high greenhouse gas emissions. *Clim. Change* **109:** 33. https://doi.org/10.1007/s10584-011-0149-y.

Rothfusz, L.P. 1990. *The heat index equation (or, more than you ever wanted to know about heat index)*. Forth Worth, TX: NWS Southern Region Headquarters.

Rosenthal, J.K., P.L. Kinney & K.B. Metzger. 2014. Intra-urban vulnerability to heat-related mortality in New York City, 1997–2006. *Health Place* **30:** 45–60.

Rosenzweig, C. & W. Solecki. 2018. Action pathways for transforming cities. *Nature Clim. Change* **8:** 756–759. doi:https://doi.org/10.1038/s41558-018-0267-x.

Ryu, Y.H., J.A. Smith, E. Bou-Zeid & M.L. Baeck. 2016. The influence of land surface heterogeneities on heavy convective rainfall in the Baltimore–Washington metropolitan area. *Mon. Weather Rev.* **144:** 553–573.

Sailor, D.J. 2001. Relating residential and commercial sector electricity loads to climate—evaluating state level sensitivities and vulnerabilities. *Energy* **26:** 645–657.

Sagarika, S., A. Kalra, S. Ahmad. 2014. Evaluating the effect of persistence on long-term trends and analyzing step changes in streamflows of the continental United States. *J. Hydrol.* **517:** 36.

Salamanca, F., A. Krpo, A. Martilli & A. Clappier. 2010. A new building energy model coupled with an urban canopy parameterization for urban climate simulations—part I. Formulation, verification, and sensitivity analysis of the model. *Theor. Appl. Climatol.* **99:** 331–344.

Sanders, B.F., J.E. Schubert & H.A. Gallegos. 2008. Integral formulation of shallow-water equations with anisotropic porosity for urban flood modeling. *J. Hydrol.* **362:** 19–38.

Santamouris, M. 2014. On the energy impact of urban heat island and global warming on buildings. *Energy Build.* **82:** 100–113.

Schaeffer, R. *et al.* 2012. Energy sector vulnerability to climate change: a review. *Energy* **38:** 1–12.

Screen, J.A. & I. Simmonds. 2010. The central role of diminishing sea ice in recent arctic temperature amplification. *Nature* **464:** 1334. https://doi.org/10.1038/nature09051 https://www.nature.com/articles/nature09051#supplementary-information.

Screen, J.A., C. Deser & L. Sun. 2015. Reduced risk of North American cold extremes due to continued arctic sea ice loss. *Bull. Am. Meteorol. Soc.* **96:** 1489–1503.

Screen, J.A., T.J. Bracegirdle & I. Simmonds. 2018. Polar climate change as manifest in atmospheric circulation. *Curr. Clim. Change Rep.* **4:** 383–395.

Seneviratne, S.I., D. Lüthi, M. Litschi & C. Schär. 2006. Land–atmosphere coupling and climate change in Europe. *Nature* **443:** 205–209.

Sen, P.K. 1968. Estimates of the regression coefficient based on Kendall's tau. *J. Am. Statist. Assoc.* **63:** 1379–1389.

Seo, B.C., W.F. Krajewski, A. Kruger, *et al.* 2011. Radar-rainfall estimation algorithms of Hydro-NEXRAD. *J. Hydroinf.* **13:** 277–291.

Shepherd, J.M. 2013. Impacts of urbanization on precipitation and storms: physical insights and vulnerabilities. *Clim. Vulnerability* **5:** 109–125.

Shepherd, J.M. 2005. A review of the current investigations of urban-induced rainfall and recommendations for the future. *Earth Interact.* **9: 1**.

Shepherd, J.M., H. Pierce & A.J. Negri. 2002. Rainfall modification by major urban areas: observations from spaceborne rain radar on the TRMM satellite. *J. Appl. Meteorol.* **41:** 689–701.

Skamarock, W., J. Klemp, J. Dudhia, *et al.* 2008. A description of the advanced research WRF version 3. https://doi.org/10.5065/D68S4MVH. https://doi.org/10.5065/D68S4MVH.

Small, D., S. Islam & R.M. Vogel. 2006. Trends in precipitation and streamflow in the eastern US: paradox or perception? *Geophys. Res. Lett.* **33:** L03403. https://doi.org/10.1029/2005GL024995.

Smith, B. & S. Rodriguez. 2017. Spatial analysis of high-resolution radar rainfall and citizen-reported flash flood data in ultra-urban New York City. *Water* **9:** 736.

Smith, B.K. & J.A. Smith. 2015. The flashiest watersheds in the contiguous United States. *J. Hydrometeorol.* **16:** 2365–2381.

Smith, B.K., J.A. Smith, M.L. Baeck, *et al.* 2013. Spectrum of storm event hydrologic response in urban watersheds. *Water Resour. Res.* **49:** 2649–2663.

Smith, J.A., M.L. Baeck, G. Villarini, *et al.* 2012. Analysis of a long-term, high-resolution radar rainfall data set for the Baltimore metropolitan area. *Water Resour. Res.* **48:** 1–14.

Smith, A., N. Lott & R. Vose. 2011. The integrated surface database: recent developments and partnerships. *Bull. Amer. Meteor. Soc.* **92:** 704–708.

Steinschneider, S. & C. Brown. 2012. Dynamic reservoir management with real-option risk hedging as a robust adaptation to nonstationary climate. *Water Resour. Res.* **48:** W05524.

Stockton, C.W. & G.C. Jacoby. 1976. Long-term surface-water supply and streamflow trends in the Upper Colorado River basin based on tree-ring analyses. *Lake Powell Res. Project Bull.* **18:** 70.

Taha, H. 1997. Urban climates and heat islands: albedo, evapotranspiration, and anthropogenic heat. *Energy Build.* **25:** 99–103.

Taha, H., H. Akbari, A. Rosenfeld & J. Huang. 1988. Residential cooling loads and the urban heat island—the effects of albedo. *Build. Environ.* **23:** 271–283.

Taylor, K.E., R.J. Stouffer & G.A. Meehl. 2012. An overview of CMIP5 and the experiment design. *Bull. Amer. Meteor. Soc.* **93:** 485–498. https://doi.org/10.1175/BAMS-D-11-00094.1.

Tewari, M. *et al.* 2004. Implementation and verification of the unified NOAH land surface model in the WRF model. In *20th Conference on Weather Analysis and Forecasting/16th Conference on Numerical Weather Prediction*, Seattle, WA, 11–15.

Thibeault, J.M. & A. Seth. 2014. Changing climate extremes in the Northeast United States: observations and projections from CMIP5. *Clim. Change* **127**. https://doi.org/10.1007/s10584-014-1257-2.

Thomson, A.M. *et al.* 2011. RCP4.5: a pathway for stabilization of radiative forcing by 2100. *Clim. Change* **109:** 77. https://doi.org/10.1007/s10584-011-0151-4.

Towey, K.L., J.F. Booth, A. Frei & M.R. Sinclair. 2018. Track and circulation analysis of tropical and extratropical cyclones that cause strong precipitation and streamflow events in the New York City watershed. *J. Hydrometeorol.*

Trenberth, K.E., A. Dai, R.M. Rasmussen & D.B. Parsons. 2003. The changing character of precipitation. *Bull. Am. Meteor. Soc.* **84:** 1205–1217.

U.S. Census Bureau. 2018. QuickFacts New York City, New York. Accessed June 15, 2018. https://www.census.gov/quickfacts/fact/table/newyorkcitynewyork#viewtop.

USGS. 2018. Office of the Delaware river master, flexible flow management program (FFMP2017). Accessed June 15, 2018. https://webapps.usgs.gov/odrm/.

Vavrus, S., J.E. Walsh, W.L. Chapmanc & D. Portis. 2006. The behavior of extreme cold air outbreaks under greenhouse warming. *Int. J. Climatol.* **26:** 1133–1147.

Villarini, G., F. Serinaldi, J.A. Smith & W.F. Krajewski. 2009. On the stationarity of annual flood peaks in the continental United States during the 20th century. *Water Resour. Res.* **45:** W08417. https://doi.org/10.1029/2008WR007645.

Wahl, T., S. Jain, J. Bender, *et al.* 2015. Increasing risk of compound flooding from storm surge and rainfall for major US cities. *Nat. Clim. Change* **5:** 1093–1097.

Walsh, J., D. Wuebbles, K. Hayhoe, *et al.* 2014. Our changing climate. In *Climate Change Impacts in the United States: The Third National Climate Assessment.* J.M. Melillo, T.C. Rich-

mond & G.W. Yohe, Eds.: 19–67. U.S. Global Change Research Program. https://doi.org/10.7930/J0KW5CXT.

Weckwerth, T.M. 2000. The effect of small-scale moisture variability on thunderstorm initiation. *Mon. Weather Rev.* **128:** 4017–4030.

Westra, S., H.J. Fowler, J.P. Evans, *et al.* 2014. Future changes to the intensity and frequency of short-duration extreme rainfall. *Rev. Geophys.* **52:** 522–555.

Wilson, J.W. & D.L. Megenhardt. 1997. Thunderstorm initiation, organization, and lifetime associated with Florida boundary layer convergence lines. *Mon. Weather Rev.* **125:** 1507–1525.

Wright, D.B., J.A. Smith, G. Villarini & M.L. Baeck. 2012. The hydroclimatology of flash flooding in Atlanta. *Water Resour. Res.* **48:** 1–14.

Wright, D.B., J.A. Smith, G. Villarini & M.L. Baeck. 2013. Long-term high resolution radar rainfall fields for urban hydrology. *J. Am. Water Resour. Assoc.* **50:** 713–734.

Woodhouse, C.A., S.T. Gray & D.M. Meko. 2006. Updated streamflow reconstructions for the Upper Colorado River basin. *Water Resour. Res.* **42:** W05415. https://doi.org/10.1029/2005WR004455.

Yang, L., J.A. Smith, D.B. Wright, *et al.* 2013. Urbanization and climate change: an examination of nonstationarities in urban flooding. *J. Hydrometeorol.* **14:** 1791–1809.

Yeung, J.K., J.A. Smith, G. Villarini, *et al.* 2011. Analyses of the warm season rainfall climatology of the northeastern US using regional climate model simulations and radar rainfall fields. *Adv. Water Res.* **34:** 184–204.

Zhang, P., Y. Wu, I.R. Simpson, *et al.* 2018. A stratospheric pathway linking a colder Siberia to Barents-Kara Sea, sea ice loss. *Sci. Adv.* **4**. https://doi.org/10.1126/sciadv.aat6025.

Zhang, R., Z.Y. Chen, C.Q. Ou & Y. Zhuang. 2017. Trends of heat waves and cold spells over 1951–2015 in Guangzhou, China. *Atmosphere* **8:** 37. https://doi.org/10.3390/atmos8020037.

Appendix 2.A. NPCC3 Global Climate Models

Table 2.A.1. Global climate models used in NPCC3 ensemble for extreme heat and humidity

Center	Model
Commonwealth Scientific and Industrial Research Organization—Bureau of Meteorology (Australia)	ACCESS1-0
	ACCESS1-3
Canadian Centre for Climate Modeling and Analysis (Canada)	CanESM2
National Center for Atmospheric Research (USA)	CCSM4
Centro Euro-Mediterraneo per i Cambiamenti Climatici (Italy)	CMCC-CM
	CMCC-CMS
Centre National de Recherches Météorologiques/Centre Eurorpéen de Rechercheet Formation Avencée en Calcul Scientifique (France)	CNRM-CM5
Commonwealth Scientific and Industrial Research Organization/Queensland Climate Change Centre of Excellence (Australia)	CSIRO-Mk3-6-0
NOAA Geophysical Fluid Dynamics Laboratory (USA)	GFDL-ESM2G
	GFDL-ESM2M
NASA Goddard Institute for Space Studies (USA)	GISS-CM3
	GISS-E2-H
	GISS-E2-R
Met Office Hadley Centre (UK)	HadGEM2-AO
	HadGEM2-CC
	HadGEM2-ES
Institut Pierre-Simon Laplace (France)	IPSL-CM5A-LR
	IPSL-CM5A-MR
	IPSL-CM5B-LR
Japan Agency for Marine-Earth Science and Technology, Atmosphere and Ocean Research Institute/National Institute for Environmental Studies/Japan Agency for Marine-Earth Science and Technology (Japan)	MIROC-ESM
	MIROC-ESM-CHEM
	MIROC5
Max Planck Institute for Technology (Germany)	MPI-ESM-LR
	MPI-ESM-MR
Meteorological Research Institute (Japan)	MRI-CGCM3
Institute for Numerical Mathematics (Russia)	INM-CM4

Appendix 2.B. NPCC3 Bias Correction Methods for Heat Waves

The bias correction technique corrects for both differences in model mean and standard deviation using a linear model, or:

$$T_{BC} = \overline{T}_{Obs,REF} + \frac{\sigma_{Obs,REF}}{\sigma_{GCM,REF}} \left(T_{GCM,RAW}(t) - \overline{T}_{GCM,REF} \right)$$

TBC refers to the bias-corrected temperature record. In the equation, T refers to the temperature records, and σ refers to the standard deviation of temperatures. Subscripts *Obs* and *GCM* refer to observations and climate model data, respectively, while *REF* and *RAW* refer to the reference (2006–2015) and entire projection periods (2006–2099), respectively. The over bar (–) marker denotes use of the average for the specified dataset and time period. The calculation of the bias correction is performed by weighting the difference between the observed reference and total period data by the ratio of the observed to climate model standard deviations, and adding the "weighted difference" to the observations to produce a time series.

The mean values of the four urban stations are used as observations for the training period of 2006–2015 for each model of the ensemble. The correction is then carried on for the three 30-year periods of interest (2020s, 2050s, and 2080s). The bias-corrected distributions are presented in Figure 2.B.1 for the complete ensemble of GCM daily maximum temperatures, which shows the bias-corrected distributions are much closer to the observations.

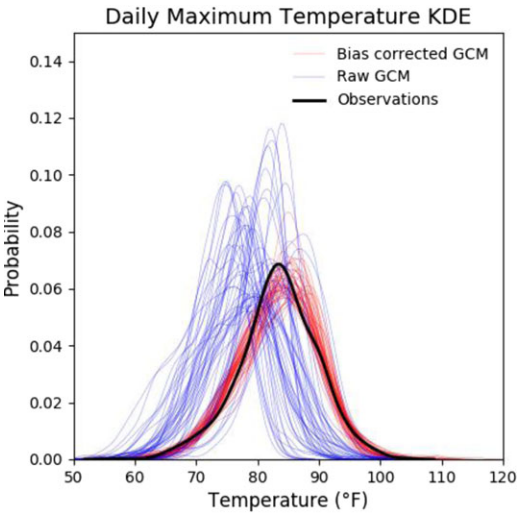

Figure 2.B.1. Sample of bias-corrected GCM distributions for maximum temperatures for the training period of 2006–2015. KDE refers to a Kernel Density Estimate, a representation of the probability of occurrence of a given value in the data set.

Appendix 2.C. Potential New Methods for NPCC4 Extreme Heat Projections

The output from GCMs can be dynamically downscaled, in which GCM outputs are used to drive high-resolution RCMs. This approach has led to development of regional, or limited area models (Dickinson *et al.*, 1989; Giorgi *et al.*, 1993; Skamarock *et al.*, 2008). This is a potential method for the next generation of NPCC climate change projections for New York City for use in adaptation planning and implementation. It can be a useful approach because GCMs used for quantifying future changes currently do not have adequate resolution to realistically simulate many extreme weather events, such as extreme heat, tropical storms, rapidly deepening nor'easters, severe convective storms, and heavy rainfall. Since these models are often run at 100–300 km grid spacing, much of the uncertainty originates from not properly resolving atmospheric dynamics for this weather. Further, GCM physics have large uncertainties at coarse resolution, since they do not resolve finer-scale processes such as the UHI and sea breezes. See Tables 2.C.1 and 2.C.2 for details.

Dynamical downscaling uses output from GCMs as initial and boundary conditions for high-resolution model run centered on the region of interest. In order to resolve clouds and urban-specific processes (e.g., anthropogenic heat and radiation blocking), this will require resolutions

Table 2.C.1. Summary of approach used for regional climate model simulations

Simulation approach	
Regional Climate Model	Weather Research and Forecasting (WRF) model version 3.8
Initial and boundary conditions	Community Earth System Model version 1 (CESM1)
Baseline years	2006–2010
Simulation period	June 1st to August 31st
Scenarios	RCP4.5 (medium emissions) RCP8.5 (high emissions)

Table 2.C.2. Physics options used in WRF simulations

Parameterization	Reference
Convection	Kain-Fritsch (Kain, 2004)
Microphysics	WSM6 (Hong and Lim, 2006, p. 6)
Boundary Layer	Mellow-Yamada-Janjic (Nakanishi and Niino, 2006)
Land Surface	Noah land surface model (Tewari *et al.*, 2004)
Urban Physics	BEP (Martilli *et al.*, 2002) BEM (Salamanca *et al.*, 2010) Cooling Tower (Gutiérrez *et al.*, 2015b) Urban Drag Coefficient (Gutiérrez *et al.*, 2015a)

around 4-km grid spacing or less; however, most current downscaling simulations use ∼20-km grid spacing. To address uncertainties in dynamically downscaled simulations, multi-simulation ensembles are employing varying boundary conditions, physics parameterizations, and grid spacing should be employed. Examples of this ensemble approach include the North American Regional Climate Change Assessment Program (NARCCAP; Mearns *et al.*, 2009) for the contiguous United States at 50 km resolution.

Another approach is using pseudo-global warming (PGW; Kimura and Kitoh, 2007). In the PGW approach, the ensemble mean monthly temperature changes from the GCMs are added to the historical reanalysis data, which in turn is used for initial conditions (ICs)/boundary conditions (BCs) for the future high-resolution regional domain runs. This approach is cheaper, since separate runs are not needed for each GCM, but this approach does not include any large-scale flow changes in the future from the GCM, since only temperature perturbations are added.

2.C.1 High-resolution dynamical downscaling

To test the approach for the New York metropolitan region, GCM projections are downscaled using an urbanized version of the Weather Research and Forecast Model (WRF; Skamarock *et al.*, 2008) developed and maintained by the National Center for Atmospheric Research (NCAR). Model physics are based on Gutiérrez *et al.* (2015a; Gutiérrez *et al.* (2015b)) and are summarized in Table 2.C.2. In contrast to GCMs, dynamical downscaling is performed by embedding, or nesting, models of higher spatial complexity within each other. In this case, three domains (one parent, two nested) are used, with horizontal grid spacing of 9, 3, and 1 km (Fig. 2.C.1). The high-resolution domain covers the New York metropolitan region with results presented for New York City.

Urban parameterizations require use of urban canopy parameters, such as urban land use, building

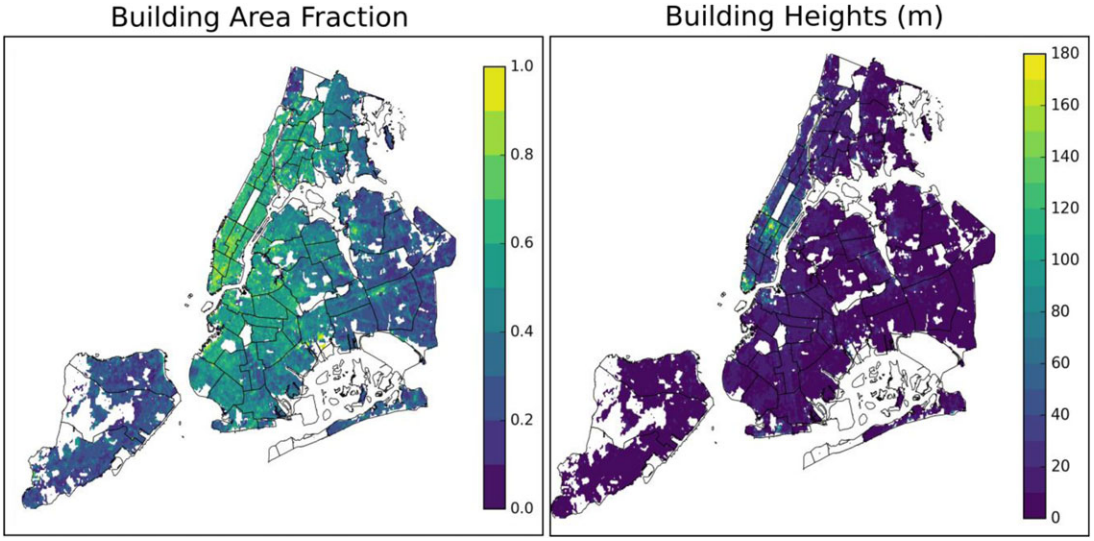

Figure 2.C.1. Urban canopy parameters for NYC derived from PLUTO. These parameters are used to calculate interactions between the atmosphere and buildings.

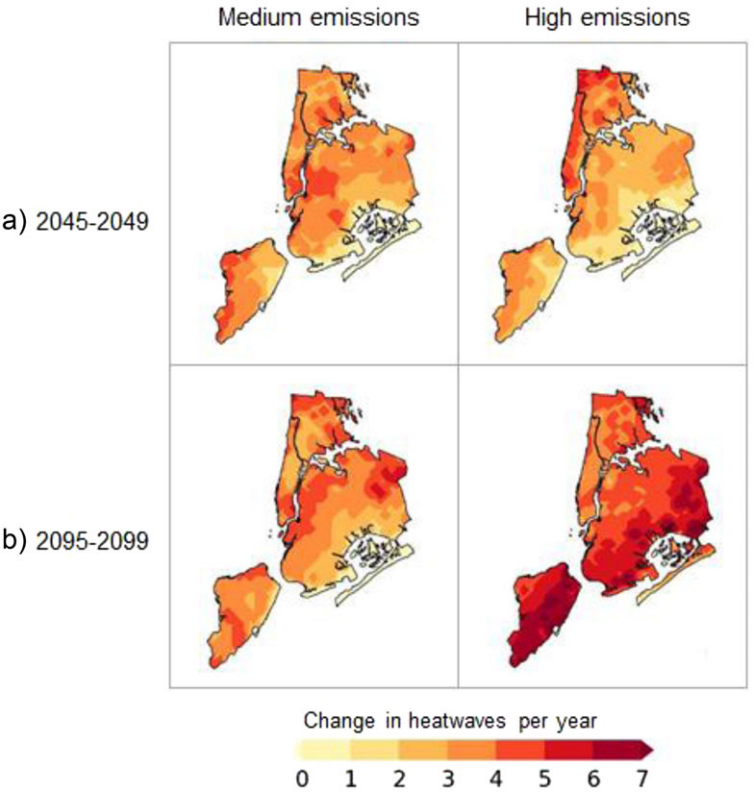

Figure 2.C.2. Median projections of event frequency for New York City.

plant area fraction (Fig. 2.C.1, left), and building heights (Fig. 2.C.1, right) to represent energy and momentum exchanges between the atmosphere and built environment (Fig. 2.C.1). These parameters have been derived from the Property Land Use Tax-lot Output (PLUTO) (NYC Open Data. Primary Land Use Tax Lot Output (PLUTO). https://data.cityofnewyork.us/City-Government/Primary-Land-Use-Tax-Lot-Output-PLUTO-/xuk2-nczf/data.) made publicly available since 2013.

Model initial and boundary conditions are taken from a bias-corrected Community Earth System Model (CESM) data set provided by NCAR (Bruyère *et al.*, 2015), which corrects biases in the intra-annual variation for all meteorological variables using ERA-Interim Reanalysis. The bias correction technique follows the work from Holland *et al.* (2010) as applied by Bruyère *et al.* (2014). The correction method separates the GCM and reanalysis signal into a seasonally varying term and a perturbation term (containing the model's climate signal). The seasonal mean is the corrected mean using the reanalysis's historical seasonally varying mean, while keeping the model's climate perturbation. This method was found by Bruyère *et al.* (2014) to produce more realistic patterns of wind shear and tropical cyclone generation for the historic period. The projection ensemble is summarized in Table 2.C.1. Correcting all model variables was shown to decrease CESM1 cold temperature biases when used as input to a regional model. Finally, three time periods are selected[f]: historical (2006–2010), mid-century (2045–2049), and end of century (2095–2099).

2.C.2 RCM results

Spatial variation of heat wave changes is shown for two time slices (2045–2049 and 2095–2099;

[f] Current computational power limits high-resolution RCM simulations to relatively time slices compared to those presented at the GCM level. However, the authors feel that the added spatial granularity provide significant value.

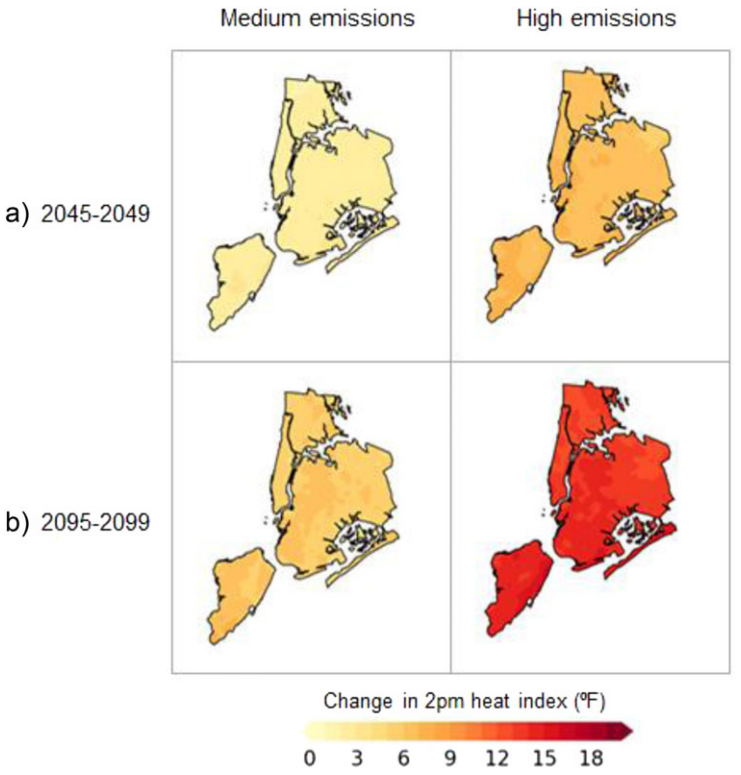

Figure 2.C.3. Median 2 pm afternoon heat index for 2045–2049 and 2095–2099 periods compared to the 2006–2010 baseline.

Fig. 2.C.2) for a typical year (i.e., median values). In general, sea breeze fronts, which typically develop in the afternoon due to land-ocean air temperature differences, play a crucial role in determining projected changes by moderating high temperatures near the coast.

The RCM simulations show that the number of heat waves per year is projected to stabilize after 2045 in the medium-emissions scenario. This stabilization occurs because the land surface warms more than the ocean and this differential warming causes sea breezes to moderate the number of heat waves that take place. This is similar to current conditions in which sea breeze circulations prevent parts of Brooklyn and Queens from experiencing as many and as severe heat waves as parts of Manhattan and the Bronx. Projections for Manhattan and The Bronx, however, show increases in heat waves by two to four events per year for both time periods.

In the high-emissions scenario (RCP8.5), the sea breeze is weakened due to increased ocean air temperatures, leading to Brooklyn and Queens experiencing higher event frequencies of between five and seven additional events per year. This is even greater than projected heatwave increases in Manhattan and The Bronx of four to six events. Larger increases near the coast may also be due to historically lower temperatures due to the local sea breeze.

The heat index (Rothfusz, 1990), combining temperature and relative humidity, is often used as a metric of how heat affects humans. Projections show that the heat index is expected to increase with time across projections, with end of century changes ranging between 6 and 8 °F in medium-emissions scenario to 12–16 °F in high-emissions scenario (Fig. 2.C.3). Changes in heat index are, in general, slightly larger over Manhattan and the northern part of Brooklyn in all scenarios and time slices except in end-of-century high-emissions scenario, where a similar pattern as that observed in event frequency projections emerges, with heat index increasing at a faster rate toward the coast.

Although multimodel high-resolution ensembles were not used in this study due to computational cost, changes in internal model variability across time slices and emissions scenarios are explored.

Table 2.D.1. Association of daily precipitation extremes at New York metropolitan region airports from 1979 to 2016

Storm type	JFK Airport station	LaGuardia Airport station	Newark Airport station
Extratropical cyclones	92, 4, 7.4%	92, 3, 7.3%	96, 5, 7.9%
Tropical cyclone	19, 4, 30.3%	17, 3, 27%	13, 5, 24%
Noncyclone	23	26	24

Note: When three values are given, the first is the number of isolated cyclones, the second is the number of extratropical plus tropical cyclones that occurred, the final number is the percentage of cyclone that pass within 500 km of New York City that caused extreme precipitation at the given station.

Sources of uncertainty in urban modeling may include:

- Representation of urban environment: Although this study uses relatively high-resolution urban canopy parameters, building-atmosphere interactions are heavily parameterized, depending on values averaged over grid points.
- Limited domain size: Due to computational limitations, high-resolution urban climate models run on a relatively small domain. Local conditions, in particular heat waves, are impacted by large scale synoptic processes that may occur thousands of miles away from New York City. Any uncertainties in the input model will be carried over in boundary and initial conditions used in these simulations.

Appendix 2.D. Methods of Extreme Rainfall Analyses

Table 2.D.1 summarizes the results of the extratropical and tropical cyclone associated analysis. If neither type of cyclone was associated with the precipitation event, the event is labeled noncyclone. In addition to identifying the total number of cyclone-associated events, we calculate the percentage of cyclones that cause extremes. To do this, we divide the number of cyclones associated with a precipitation extreme by the total number of cyclones that pass within 500 km of New York City. For extratropical cyclones, 7.5% of the storms caused a precipitation extreme. For tropical cyclones, the number is much higher, at 30%. This probabilistic calculation cannot be made for noncyclones, because the storm-type for those events is not known. At least some of those events are most likely associated with are quasi-linear convective systems (Lombardo and Colle, 2012), which are sometimes grouped with frontal systems (Kunkel *et al.*, 2011). The dominant cause of extreme daily rainfall events for all airport stations out of these storm types is extratropical cyclones.

Radar was processed with the Hydro-NEXRAD algorithms (Seo *et al.*, 2011) and corrected with

Table 2.D.2. Statistical analyses of rainfall data in New York City region

Parameter		CP	LGA	EWR	JFK
Hourly record	Time period	1948–2013	1948–2013	1948–2013	Hourly record
One hour	Change point	–	–	1971 (+35%)**	One hour
	Trend	–	–	–	
Three hours	Change point	1967 (+42%)**	–	–	Three hours
	Trend	–	–	0.2 mm/year**	
Six hours	Change point	1966 (+34%)**	–	–	Six hours
	Trend	–	–	–	
Daily	Change point	1965 (+17%)**	–	1971 (+30%)**	Daily
	Trend	–	–	–	
Daily record	Time period	1869–2017	1940–2017	1893–2017	Daily record

Note: Rainfall gauges located at Central Park, LaGuardia Airport, Newark Airport, and JFK Airport. Statistics are for 1-, 3-, 6-h, and daily annual rainfall maxima. Change points are shown in year and (change in averages), while trends are shown in Sen's Slope.
** A value is significant at a 5% level.
* A value is significant at a 10% level.

Table 2.D.3. Statistical analyses of streamflow data in the U.S. census New York City urban region

USGS gauge ID	Location	Time frame	Number of years	Change point	Trend (cfs/year)	Notes
01374654	Carmel, NY	1996–2012	17	–	–	Regulated flow
01374930	Baldwin Place, NY	1996–2016	21	2011 (–38%)*	–	Occasional regulation
01381400	Morristown, NJ	1996–2015	20	–	–	Diversion upstream
01387450	Suffern, NY	1959–1998	40		–	
		2001–2015	15	1967 (+154%)**		Well withdrawals upstream
01392210	Passaic, NJ	1977–1999	21	–	–	
01399670	Whitehouse Station, NJ	1978–2015	37	–	14.09*	Occasional regulations and upstream releases
01401650	Belle Mead, NJ	1991–2015	25	–	–	Some irrigation regulation in summer
01403150	Martinsville, NJ	1980–2015	35	–	3.84*	
01403400	Seeley Mills, NJ	1967–2015	49	–	–	Temporarily moved 1969–1979
01403535	Watchung, NJ	1980–2015	36	–	–	
01403540	Watchung, NJ	1973–2015	43	–	–	Occasional regulation, channel modified in 1991 and 1997
01407290	Marlboro, NJ	1980–2015	35	1999 (–25%)*	–	
01407705	Neptune City, NJ	1967–2014	48	–	–	Diversion upstream, a portion is regulated
01407760	Neptune City, NJ	1967–2016	50	–	–7.47**	Upstream diversion water supply and golf courses

Note: Statistics are for annual peak (maximum) in instantaneous streamflow. Change points are shown in year and (change in averages), while trends are shown in Sen's Slope.
** A value is significant at a 5% level.
* A value is significant at a 10% level.

a daily multiplicative bias (as in Smith *et al.*, 2012) using rain gauges from the National Oceanic and Atmospheric Administration Meteorological Assimilation Data Ingest system (NOAA MADIS, https://madis.ncep.noaa.gov).

Methods for determining trends in extreme rainfall and proxy-stream flash flooding included the nonparametric Pettitt Test (Pettitt, 1979), nonparametric Mann-Kendall Test (Mann, 1945, Kendall, 1975), and Sen's Slope (Sen, 1968). Complete results from these analyses are shown in Tables 2.D.2 and 2.D.3.

Appendix 2.E. Methods of Tree Ring Analysis and Drought Analysis

The PCN reservoir inflows were developed using a Bayesian regression model. Given data from three streamflow gages and eight local tree-ring chronologies (that date back to 1754) as predictor variables, the Bayesian model provides regression equations for each reservoir that are used to hindcast the streamflow. Annual average daily streamflow (June–May) was assumed to follow a lognormal distribution. The Bayesian regression models used to produce this partially pooled reconstruction explain around 60% of the streamflow variance and validate best against withheld data. The posterior probability distributions of the reconstructed combined reservoir inflow from the Bayesian regression model during the period 1754–2000 are shown in Figure 2.13. The record period common to all selected trees determined the time span of the reconstructions. The reconstructions of the combined reservoir inflow are presented as time series composed of the

Table 2.E.1. Summary of the probability of exceedances and the return periods of the droughts for four different demand levels

		Demand			
		950 MGD $D^* = 6$ $S^* = 1000$ MGD	1000 MGD $D^* = 6$ $S^* = 1300$ MGD	1050 MGD $D^* = 6$ $S^* = 1600$ MGD	1100 MGD $D^* = 7$ $S^* = 1900$ MGD
Exceedance probability	$P(S > S^*)$	0.03	0.04	0.45	0.95
	$P(D > D^* \cap S > S^*)$	0.006	0.028	0.40	0.94
Return period	Severity	33 years	25 years	2.2 years	1 years
	Joint	166 years	36 years	2.5 years	1 year

median of the posterior distribution for each year, as the reconstructions for each year are estimates of the posterior distribution of the annual average daily inflow for those years. The record of observed PCN combined inflow data is shown using the 11-year low-pass filtered values (blue color line during the instrumental period (1928–2000)). Similar low-pass filtered values are also shown for the median inflows (red color line) during the reconstruction period to visualize the general trend in the data.

2.E.1. *Drought index (methods)*

We developed the drought index to capture the effect of drought over multiple years. The index is based on the sequent peak algorithm (Loucks *et al.*, 1981). It quantifies the water reservoir drawdown for meeting the demand. The steps for the computation are as follows:

$$\text{Deficit}_t = \max(\text{Deficit}_{t-1} + D_t - S_t, 0),$$

$$\text{where Deficit}_{t=0} = 0$$

$$\text{Severity} = \max_t(\text{Deficit}_t; t = 1 : n - \text{years}).$$

where Deficit_t refers to the accumulated annual deficit, D_t refers to the annual water demand, S_t refers to the annual water supply and n is the total number of years under considerations. The maximum accumulated deficit estimated over the n-year period is defined as the Severity of the drought. It measures the potential impact of multiyear droughts (Etienne *et al.*, 2016).

2.E.2. *Drought profile based on the reconstructed reservoir inflow data*

The demand-specific drought index is applied to the simulations of the reconstructed PCN combined

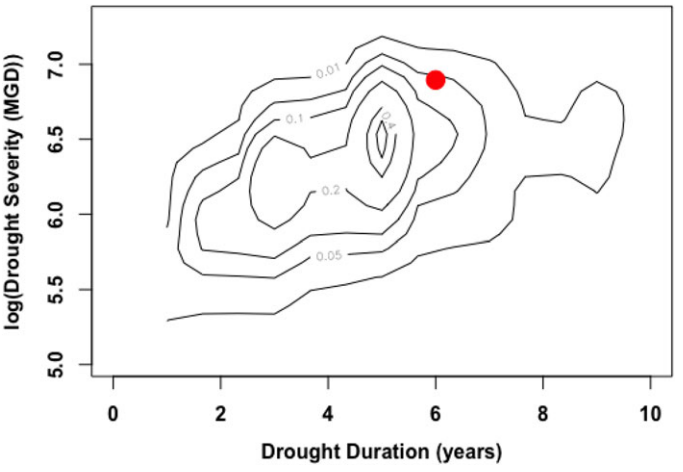

Figure 2.E.1. The joint drought profile for a demand of 950 MGD annual average daily outflow. The contour plot shows the joint probability distribution of drought duration and severity. The drought of the record (1960s drought of 6 years and 1000 MGD cumulative deficit) is shown as a red circle on the contour plot.

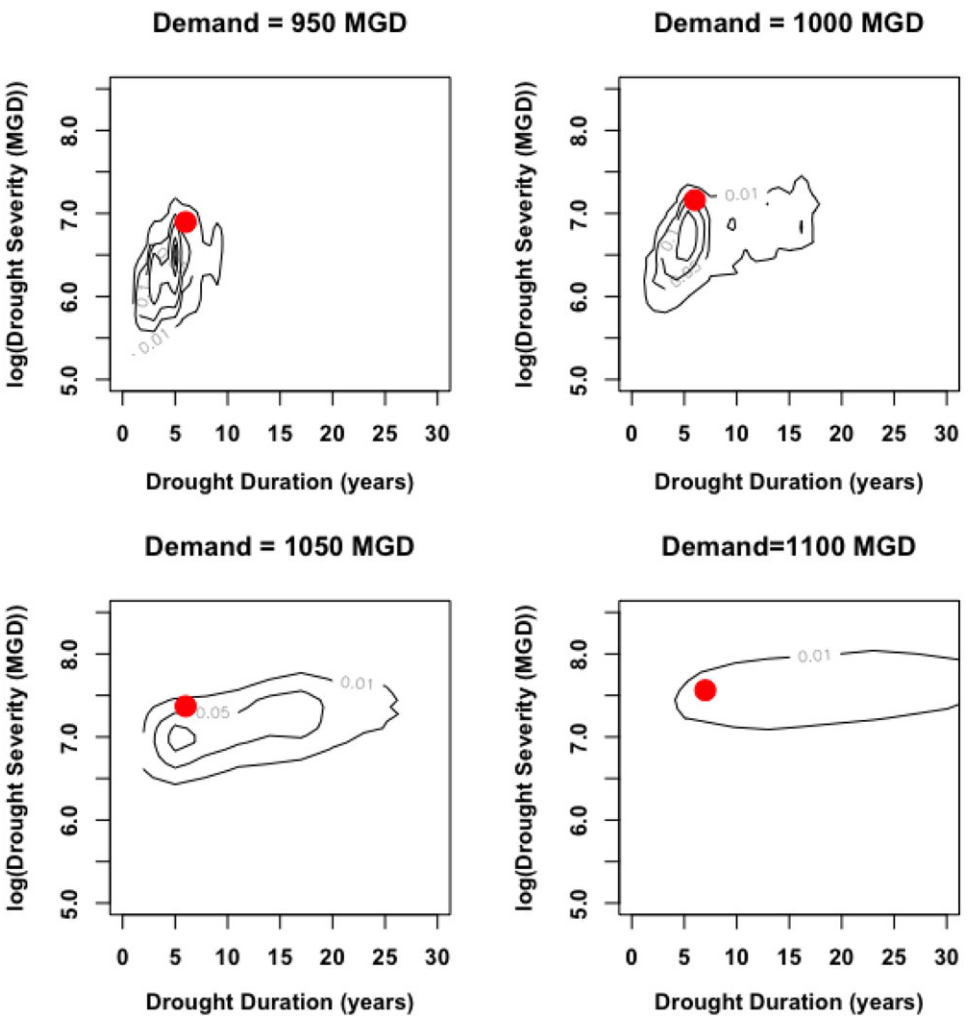

Figure 2.E.2. The joint drought profile for varying demands.

inflows with a demand threshold of 950 million gallons per day (MGD) of annual average daily flow to develop the long-term drought risk profile. Figure 2.E.1 presents the joint probability distribution of the drought duration and severity as seen from the paleo records. The worst drought event in the instrumental period (the 1960s drought of 6 years and a cumulative deficit of 1000 MGD) is shown as a red circle in the figure. It is evident from the paleo streamflow data that the drought of the record, the 1960s drought, is still an extreme event relative to a long-term drought risk profile. The probability of exceedance of the 6-year drought duration is $P(\text{Duration} > 6) = 0.06$, an approximate average return period of 16 years if drought length is of concern. The probability of exceedance of the 1000 MGD cumulative deficit (drought severity) is $P(\text{Severity} > 1000\,\text{MGD}) = 0.03$, an approximately average return period of 33 years if drought severity is of concern. However, if combined variables of duration and severity are of interest, the probability of joint exceedance $P(\text{Duration} > 6 \cap \text{Severity} > 1000) = 0.006$, an approximate average return period of 166 years. Hence, while a drought of a 6-year length occurs more frequently than the drought of a 1000 MGD severity, the recurrence of the joint drought as worse as the 1960s is anomalous.

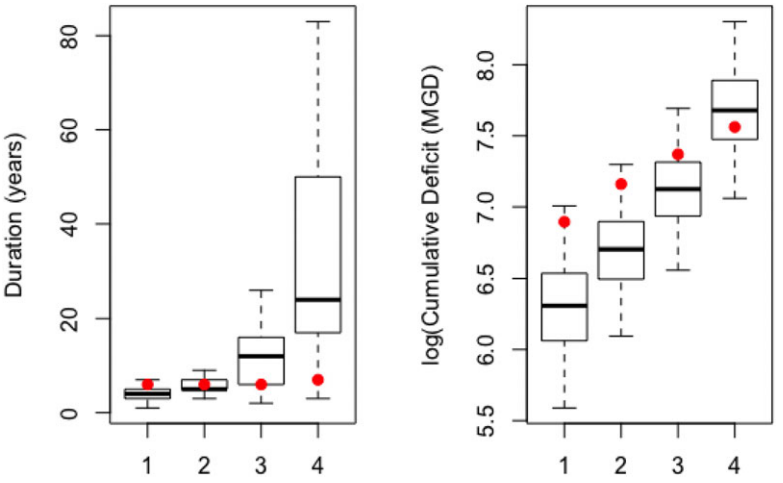

Figure 2.E.3. The distributions of drought duration and severity for varying demands.

2.E.3. Drought profile based on the reconstructed reservoir inflow data and changing demand

It is important to note that the drought stress is always relative to the demand of the region. The above analysis is shown for a demand of 950 MGD of annual average daily flow as a benchmark water demand. We have chosen this threshold given this is the average PCN combined reservoir release (including diversions to New York City, conservation, and directed releases) for the last 5 years (USGS, 2018). To investigate the effect of water demand on drought stress, we have applied the drought index for four different thresholds, 950 MGD, 1000 MGD, 1050 MGD and 1100 MGD. Any average demand greater than 1100 MGD will exceed the average combined reservoir inflow.

The joint probability distributions of drought duration and drought severity (long-term drought profiles) for various water demand levels is shown in Figure 2.E.2. We observe from these distributions that the drought duration is changing at a rate faster than the drought severity with increasing demand. As the water demand of the region increases, from a

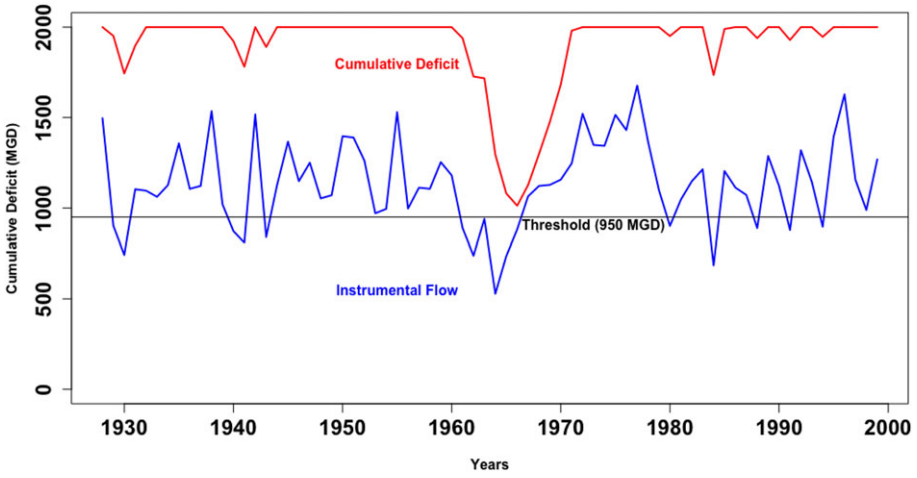

Figure 2.E.4. Annual average daily inflows and cumulative deficit (drawdown) of the combined Pepacton, Cannonsville, and Neversink (PCN) reservoir during the instrumental period (1928–2000). The blue line shows the observed PCN reservoir combined inflow. The red line (inverted) indicates the cumulative deficit.

long-term planning perspective, the critical metric to focus on will be the length of drought. Drought stress is experienced in terms of its persistence. This can also be seen from Figure 2.E.3, which shows the individual distributions for each of these thresholds along with the drought of the record from the instrumental period.

The streamflow reconstructions reveal droughts with a longer duration than the duration of the drought seen in the instrumental period (1960s drought). Joint distributions of duration and severity are developed for various demand levels to get a better perspective of the long-term drought profile. Based on a demand level that matches the average reservoir releases for the last 5 years, the worst drought of the record in the instrumental period is 6-year drought with a 1000 MGD cumulative deficit. This event has a joint return period of 166 years when contextualized with the long-term drought profile. However, the drought stress is very sensitive to regional water demand. A marginal increase in the demand from the 950 MGD level will lead to droughts that are longer and more severe, and their joint occurrence becomes more frequent. A comparison of duration versus severity metrics indicates that the rate of change with respect to demand levels is much faster for the drought duration.

2.E.4. Observed droughts

For the period of 1928–2000, annual average daily inflows and cumulative reservoir deficit was calculated based on a total demand of 950 MGD of annual average daily flow (Fig. 2.E.4). Note that 950 MGD is approximately the average reservoirs' release for the recent 5 years.

In the decade of the 1960s, the reservoirs had extensive drawdown, making it the worst drought of the instrumental period. The observed duration of the drought is 6 years, from 1961 to 1967. The severity of the drought, measured as the cumulative deficit, is approximately 1000 MGD. The recovery period of this drought is 5 years. While there are other periods with small to moderate droughts, there is no other period in the instrumental record that has a drought as severe as the 1960s drought.

Table 2.E.1 summarizes the individual and joint probability of exceedances and return periods of the drought duration and severity. Evidently, they are very sensitive to the demand. While the droughts stress for a demand level consistent with the water releases for the past 5 years is moderate, the drought stress is more likely and reoccurs more frequently for a marginal increase in the demand levels.